eNeuro

*Research Article: New Research | Development*

# Short-term Dendritic Dynamics of Neonatal Cortical Neurons Revealed by *in vivo* Imaging with Improved Spatiotemporal Resolution

https://doi.org/10.1523/ENEURO.0142-23.2023

**Cite as:** eNeuro 2023; 10.1523/ENEURO.0142-23.2023

Received: 1 May 2023
Revised: 16 September 2023
Accepted: 19 September 2023

# Short-term Dendritic Dynamics of Neonatal Cortical Neurons Revealed by *in vivo* Imaging with Improved Spatiotemporal Resolution

Abbreviated title:

Short-term Dendritic Dynamics of Neonatal Neurons

Luwei Wang[1,2], Shingo Nakazawa[1], Wenshu Luo[1], Takuya Sato[1], Hidenobu Mizuno[3], Takuji Iwasato[1,2]

1. Laboratory of Mammalian Neural Circuits, National Institute of Genetics, Mishima, Japan 411-8540

2. Graduate Institute for Advanced Studies, SOKENDAI, Mishima, Japan 411-8540

3. International Research Center for Medical Sciences, Kumamoto University, Kumamoto, Japan 860-0811

Emails and addresses:

Luwei Wang: lwwang@nig.ac.jp; 1111 Yata, Mishima, Shizuoka 411-8540, Japan

Shingo Nakazawa: shingo.nakazawa@gmail.com; 1111 Yata, Mishima, Shizuoka 411-8540, Japan

Wenshu Luo: wenshuluo@hotmail.com; 1111 Yata, Mishima, Shizuoka 411-8540, Japan

Takuya Sato: tsatou@nig.ac.jp; 1111 Yata, Mishima, Shizuoka 411-8540, Japan

Hidenobu Mizuno: hmizuno@kumamoto-u.ac.jp; 2-2-1 Honjo, Chuo-ku, Kumamoto City 860-0811, Japan

Takuji Iwasato: tiwasato@nig.ac.jp; 1111 Yata, Mishima, Shizuoka 411-8540, Japan

Corresponding author: Takuji Iwasato, Laboratory of Mammalian Neural Circuits, National Institute of Genetics, Mishima, Japan 411-8540. Email: tiwasato@nig.ac.jp

Number of pages: 43

Number of figures: 9, tables: 2, and multimedia: 0

Number of words for abstract: 245, introduction: 545, and discussion: 1838

**Acknowledgments**

We thank Tatsumi Hirata, Akatsuki Kimura, Fumi Kubo, Tsuyoshi Koide, and Hiroshi Kawasaki for comments on earlier versions of the manuscript; Naoki Nakagawa for critical reading of the manuscript; Yumiko Saga, Chiemi Kimura-Nakajima, Piu Banerjee, Ayane Nihashi, Asuka Yamashita, Shota Katori, Ramasamy Kandasamy and Toshikuni Sasaoka for discussion; Minako Kanbayashi and Satoko Kouyama for technical assistance. This work was supported by MEXT KAKENHI JP20H03346, JP16H06459 and JP21K18245; and the Collaborative Research Project (2023-#23017) of Brain Research Institute, Niigata University to T.I. The authors declare no competing financial interests.

**Abstract:**

Individual neurons in sensory cortices exhibit specific receptive fields based on their dendritic patterns. These dendritic morphologies are established and refined during the neonatal period through activity-dependent plasticity. This process can be visualized using two-photon *in vivo* time-lapse imaging, but sufficient spatiotemporal resolution is essential. We previously examined dendritic patterning from spiny stellate (SS) neurons, the major type of layer 4 (L4) neurons, in the mouse primary somatosensory cortex (barrel cortex), where mature dendrites display a strong orientation bias toward the barrel center. Longitudinal imaging at 8-h intervals revealed the long-term dynamics by which SS neurons acquire this unique dendritic pattern. However, the spatiotemporal resolution was insufficient to detect the more rapid changes in SS neuron dendrite morphology during the critical neonatal period. In the current study, we imaged neonatal L4 neurons hourly for 8 h and improved the spatial resolution by uniform cell-surface labeling. The improved spatiotemporal resolution allowed detection of precise changes in dendrite morphology and revealed aspects of short-term dendritic dynamics unique to the neonatal period. Basal dendrites of barrel cortex L4 neurons were highly dynamic. In particular, both barrel-inner and barrel-outer dendrites (trees and branches) emerged/elongated and disappeared/retracted at similarly high frequencies, suggesting that SS neurons acquire biased dendrite patterns through rapid trial-and-error emergence, elongation, elimination, and retraction of dendritic trees and branches. We also found correlations between morphology and behavior (elongation/retraction) of dendritic tips. Thus, the current study revealed short-term dynamics and related features of cortical neuron dendrites during refinement.

**Significance Statement:**

The formation of proper dendritic patterns during early postnatal development is essential for normal neuronal circuit function in adulthood. To elucidate the mechanisms responsible for this

refinement, *in vivo* imaging with high spatiotemporal resolution is useful. Our previous long-term *in vivo* imaging studies have clarified aspects of dendritic refinement mechanism; however, due to the long intervals (8-h) between image acquisitions, rapid changes in dendritic morphology were missed. Here hourly *in vivo* time-lapse imaging of neonatal mouse barrel cortex over 8 h revealed the rapid changes in the dendrite morphology of layer 4 neurons, thereby providing a more comprehensive record of dendritic refinement during postnatal development for mechanistic analysis.

**Introduction:**

Complex yet precise connectivity of neurons underlies higher brain functions in mammals. The specificity of neuronal connections depends largely on dendritic patterns as they determine the inputs received by individual neurons. Mature spiny stellate (SS) neurons in the mouse primary somatosensory cortex (barrel cortex) layer 4 (L4) show highly biased basal dendritic patterns oriented toward the barrel center, where thalamocortical axons (TCAs) transmit single-whisker inputs. This unique asymmetric basal dendritic pattern, which underlies the precise one-to-one functional relationship between whiskers and barrels, is formed during neonatal stages in a TCA input-dependent manner (Datwani et al., 2002; Espinosa et al., 2009; Mizuno et al., 2014). Thus, barrel cortex SS neuron basal dendrites are an ideal model for studying the mechanisms of dendritic refinement.

To reveal the mechanisms of dendritic refinement, it is critical to elucidate the dynamic features of dendrites during early postnatal development. Two-photon microscopy has been used extensively for imaging of spine dynamics *in vivo* during late postnatal development and adulthood (Holtmaat & Svoboda, 2009; Lendvai et al., 2000; Yang et al., 2009). Some studies have also addressed axon dynamics *in vivo* (Carrillo et al., 2013; Portera-Cailliau et al., 2005; Ruthazer et al., 2003). On the other hand, understanding dendrite dynamics is largely delayed

(Mizuno et al., 2014; Nakazawa et al., 2018), which is partly because visualization of dendrite morphology *in vivo* is difficult in the neonatal brain (Ako et al., 2011; Espinosa et al., 2009; Luo et al., 2016; Young et al., 2008). We previously achieved that by developing the Supernova system, a versatile sparse cell labeling method (Luo et al., 2016; Mizuno et al., 2014), and successfully performed two-photon *in vivo* imaging of individual L4 neurons in the neonatal barrel cortex at 4 time points within 18 h between postnatal day 5 (P5) and P6 (Mizuno et al., 2014). This study analyzed morphological changes in barrel cortex L4 neuron basal dendrites in the neonatal cortex and detected dendritic motility *in vivo* for the first time. Subsequently, we achieved longitudinal *in vivo* imaging of morphological changes in basal dendrites from P3 to P6 (Nakazawa et al., 2018).

Although the aforementioned study revealed the long-term dynamics that generate orientation bias, the spatiotemporal resolution was not sufficient to capture short-term dendritic dynamics during neonatal dendritic refinement. In that study, to cover the whole refinement processes between P3 and P6, we set acquisition intervals of 8 or 24 hours. However, the changes in dendrite morphology over 8 h are much larger than expected (Nakazawa et al., 2018), which hindered the detection of rapid changes over shorter periods. For example, if a dendritic branch is eliminated and a new branch emerges at a similar position within 8 h, it could be mistakenly recognized as the same. Thus, greater temporal resolution is required to reduce such potential errors.

To characterize the short-term dynamics of SS neuron dendrites more precisely, we here conducted hourly imaging for 8 h. We also improved the spatial resolution by labeling cell surfaces with a membrane-binding fluorescent protein, which was helpful to visualize more precise dendrite morphology. In the current study, we describe the short-term dynamics of cortical neuron dendrites during the critical period of dendritic refinement. Also, we report that the elongation and retraction of dendrites were positively correlated with dendrite tip thickness.

## Materials and Methods:

### Animals

All experiments were performed according to guidelines for animal experimentation of National Institute of Genetics (NIG) and were approved by the animal experimentation committee of NIG. Thalamocortical axon (TCA)-green fluorescent protein (GFP) transgenic (Tg) mice (Mizuno et al., 2014) were backcrossed from C57BL/6J to ICR more than four times and were intercrossed to obtain TCA-GFP Tg homozygous male mice. Homozygosity of the TCA-GFP Tg mice was determined by quantitative polymerase chain reaction genotyping (qPCR) using the primers [KS89] TTCTCGTTGGGGTCTTTGCT and [KS90] ACTTCTTCAAGTCCGCCATG. To obtain pups, ICR female mice were mated with the TCA-GFP Tg homozygous male mice. The day at which the vaginal plug was detected (between 10 AM to 11 AM) was designated as embryonic day (E) 0 and E19 was defined as postnatal day (P) 0.

### Plasmids

Flpe/FRT-based Supernova vectors: pK036 (TRE-Flpe-WPRE) (Luo et al., 2016); pK037 [CAG-FRT-STOP-FRT-turbo red fluorescent protein (turboRFP)-ires-tTA-WPRE] (Luo et al., 2016), and pK300 (CAG-FRT-STOP-FRT-GAP43tagRFP-ires-tTA-WPRE) were used for sparse labeling. pK302 [CAG-blue fluorescent protein (BFP)-WPRE] (Nakazawa et al., 2020) was used for dense labeling. The plasmid DNA was purified by a Midi-prep kit (Macherey-Nagel). For the generation of pK300, the GAP43tagRFP sequence was obtained from pK190 (CAG-loxP-STOP-loxP-GAP43tagRFP-ires-tTA-WPRE) vector by SalI/EcoRV restriction digestion and inserted into SalI/EcoRV sites of pK068 (CAG-FRT-STOP-FRT-EGFP-ires-tTA-WPRE vector) (Luo et al., 2016). For the generation of pK190, GAP43 sequence (Chiaramello et al., 1996) and tagRFP sequence from pTagRFP-N vector (Haas et al., 1996; Kozak, 1987) were fused and PCR

amplified using the primers [HM67] CTAGTGTCGACATGCTGTGCTGTATGAGAAGAACCAAACAGGTTGAAAAGAATGAT GAGGACCAAAAGATCGAG and [HM75] CCGATATCTTCAATTAAGTTTGTGCCCCAGTTTGCTAGG, and then inserted into the SalI/EcoRV sites of pK038 (CAG-loxP-STOP-loxP-EGFP-ires-tTA-WPRE) vector (Luo et al., 2016).

**_In utero_ electroporation**

*In utero* electroporation (IUE) was performed on TCA-GFP Tg heterozygous mice at E14 between 10 AM and noon to label L4 neurons in the barrel cortex. The pregnant mothers were anesthetized via intraperitoneal injection of triple anesthesia (11 µg/g body weight). The triple anesthesia contains medetomidine hydrochloride (0.75 µg/g), midazolam (4 µg/g), and butorphanol tartrate (5 µg/g). A total of 0.5 µl of DNA solution (mixed with 5% methylene blue) was injected into the right lateral ventricle of embryos via a pulled glass capillary (Drummond), and square electric pulses (40 V; 50 ms) were delivered 5 times at 1 Hz by a CUY21EDIT electroporator (NepaGene). The electric pulses were given 3 times/embryo, and the current was 70–100 mA/electric pulse. After the IUE, pregnant mothers were injected with an antagonist (11 µg/g body weight), which contained atipamezole hydrochloride (0.75 µg/g), to wake them up from anesthesia and kept on a 37°C heater until they recovered from anesthesia.

For Supernova-cytosolic RFP (cRFP) labeling, a DNA solution containing pK036 (20 ng/µl) and pK037 (1 µg/µl) was used. For Supernova-membrane-bound RFP (mRFP) labeling, a DNA solution containing pK036 (20 or 40 ng/µl), pK300 (1 µg/µl), and pK302 (200 ng/µl) was used.

**_In vivo_ imaging with two-photon microscopy**

For *in vivo* imaging of L4 neurons in the barrel cortex, TCA-GFP Tg heterozygous pups at P4 were used, in which L4 neurons were labeled by IUE-based BFP and Supernova-mRFP. Mice in which L4 neurons in the barrel cortex were labeled appropriately were identified by BFP fluorescence over the skull after removing the skin from the corresponding areas. Then, the craniotomy was performed on the right half of the head while the pups were under isoflurane anesthesia (3%) as described previously (Mizuno et al., 2014; Nakazawa et al., 2018). Briefly, the skull above the IUE-labeled area in the barrel cortex was carefully removed by a razor blade with the dura remaining intact, and a small round cover glass (2.5 mm in diameter, Matsunami) was placed to cover the open skull area. Gelfoam (Pfizer) was used to stop the occasional minor bleeding and cortex buffer (Holtmaat et al., 2009) (125 mM NaCl, 5 mM KCl, 10 mM glucose, 10mM Hepes, 2 mM $CaCl_2$, and 2 mM $MgSO_4$; pH 7.4) was applied to the skull-removed area to keep the brain moist during surgery. A customized titanium bar (~30 mg) (Nakazawa et al., 2018) was attached to the adjacent area to the cranial window. No apparent surgery-induced discomfort was observed. After 1 h of recovery on a 37℃ heater with littermates, pups with cranial windows were used for *in vivo* imaging. Pups were anesthetized with isoflurane (0.9%−1.4%) and head fixed to the microscope stage using the titanium bar during *in vivo* imaging. A heating pad was used to keep the pups warm. Images were acquired using a two-photon microscope (LSM 7MP, Zeiss) with a W Plan-Apochromat 20x/1.0 DIC objective lens (Zeiss) and an LSM BiG detector (Zeiss). A HighQ-2 laser (Spectra-Physics) at 1,045 nm was used in all experiments. GFP and RFP were simultaneously excited, and the emitted fluorescence was filtered (500−550 nm for GFP and 575−620 nm for RFP). *In vivo* imaging was performed as follows: h0, h1, h2, h3, h4, h5, h6, h7, and h8 sessions started around 13:00, 14:00, 15:00, 16:00, 17:00, 18:00, 19:00, 20:00, and 21:00 at P4, respectively. Each imaging session took about 20 min. Between two imaging sessions, pups were returned to their littermates and kept on a 37°C heater. The pups usually start to respond to touch from littermates and move a few minutes after the end of the imaging session.

**Histology and confocal microscopy**

After *in vivo* imaging, brain samples were obtained and fixed with ice-cold 4% paraformaldehyde in 0.1 M phosphate buffer (PB). The brain samples were kept at 4℃ overnight and protected from light. For tangential sectioning, the right hemispheres were flattened and transferred to 30% sucrose in 0.1 M PB and kept overnight at 4℃. Tangential sections (100 µm thick) of the flattened cortices were made using a freezing microtome (ROM-380; Yamato).

Three-dimensional (3D) fluorescence images were acquired using a confocal microscope (TCS SP5; Leica). Images of the barrel map and labeled neurons were taken with a 10x/0.4 CS2 objective lens with 2x digital zoom at a step size around 2.5 µm and the total thickness was ≤ 100 µm. The 20x images were taken with 1024×1024 pixels. Images of fine structures of dendrites were taken with a 63x/1.4 oil immersion lens with 2x digital zoom at a step size around 0.1 µm and the total thickness was ≤ 100 µm. The 126x images were taken with 2048×2048 pixels. Step sizes were determined according to the optimized setting for each objective lens.

**Image analysis and quantification**

The Image J/FIJI (NIH) (version 1.53t) software was used for histological analysis. The TCA signal intensities were used to distinguish barrels and septa areas in *post hoc* analysis with confocal images (taken by a 10x lens with 2 times zoom). TCA cluster boundaries were defined as barrel edges. *In vivo* imaged L4 neurons in barrels were identified in confocal images according to their relative positions with each other and their dendritic patterns. The distance of neurons to barrel edges was defined as the distance from the center of the cell body to the nearest barrel edge, and within 20 µm were classified as edge-located neurons. Neurons located barrel inside and distances to the barrel edge longer than 20 µm were classified as barrel-center neurons and not included in the analysis of the current study.

Acquired 3D neuron images from two-photon microscopy were analyzed using the IMARIS Filament Tracer (Bitplane, version 9.5.1) software to reconstruct dendritic patterns and quantify basal dendritic morphologies. To keep the accuracy and efficiency of data analysis, we selected *in vivo* imaged neurons for analysis with the following three criteria: I, basal dendritic morphologies were clearly visible both in *in vivo* imaging (all 9 imaging sessions) and *post hoc* confocal imaging; II, neurons were located on edges of main barrels (rows A~E, arcs 1~5); III, neurons were surrounded by two (or more) main barrels. In total, 19 neurons from 3 pups satisfied the above criteria. The same "dendritic trees" and "dendritic segments" were identified from different imaging sessions. A "dendritic tree" is an extension originating from the cell body. A "dendritic segment" was defined as a segment between two branching points, or between a branching point and the origin of the dendrite (or the distal end). A primitive dendritic tree with no branches is also a dendritic segment. Newly formed and eliminated dendrite segments were detected by comparing the dendrite morphologies of the same neuron between two consecutive sessions. A 180°-barrel boundary was used to separate barrel inner and outer sides as in our previous study (Nakazawa et al., 2018). When more than half the length of a dendritic segment of a basal dendrite was located in the barrel inner side, it was defined as an "inner segment". "Orientation bias index" (OBI) = total inner segment length/total basal dendritic length. The average OBI of 9 imaging sessions from the same neuron was used as the OBI of the neuron.

For the quantification of basal dendritic tree and tip dynamics, the number of emerged, eliminated, and transient basal dendritic trees/tips from each neuron in 8 h of imaging was calculated. These dynamic events of dendritic tips were normalized with their corresponding neuron's total basal dendritic length or total inner or outer segment length (#/millimeter, mm). We classified length changes (μm) of "tip-segments" into 3 subgroups: retraction (R, length change < -3 μm), elongation (E, length change > 3 μm), and stable (length change within 3 μm), as previously reported (Mizuno et al., 2014). A "tip-segment" is defined as a dendritic segment

whose one end is a dendritic tip. A primitive dendritic tree with no branches is also a tip-segment. For the analysis of dynamics in two consecutive hours, tip-segments that were continuously existing (no formation or elimination) were selected.

To analyze the correlation of dendrite tip morphologies with its dynamics, we first investigated all basal dendritic tips of 19 neurons (h0 to h7 of imaging session) and identified 64 tips that were apparently thick. Most of these thick parts of the dendritic tips were between 5–10 µm in length. Therefore, we used the most distal 5 µm part of the dendritic tip as the tip part (T), skipped the adjacent 5 µm, and then used the subsequent 5 µm as the shaft part (S). By excluding 5 µm of the intermediate area from the analyses, we avoided overlaps between the T and S. Regions of interest (ROIs) of T and S were then determined based on the mRFP-signals at the resolution of the single pixel level. Initially, we picked out 126 tips that showed tip morphologies distinguishable from their surrounding environment with a segment length longer than 15 µm and had no overlapping with other dendrites or imaging noise. 79 out of 126 tips were continuously presented, without branching or branch elimination, in two consecutive sessions [between 1 h before (Time -1) and 1 h after (Time +1) of the TTI-checking session (Time 0)]. The mRFP signal intensity (gray value) of ROIs was analyzed with the Image J/FIJI software. The dendritic tip's "tip thickness index" (TTI) = (gray value of T)/(gray value of S). We compared TTI and the length change (µm) between Time -1 and Time +1.

**Statistical analysis**

The quantification of L4 neurons' basal dendritic dynamics was done with Microsoft Excel (Microsoft 365). The statistical analyses of dynamics comparisons were performed with GraphPad Prism (version 9.3.1). The significance of the comparisons was assessed by the Mann-Whitney test, Wilcoxon matched-pairs signed rank test, or paired t-test. Values are given as mean ± standard error of the median (SEM). The asterisks in the figures indicate the following: *$p < 0.05$, **$p < 0.01$, ***$p < 0.001$, and ****$p < 0.0001$. When $p>0.05$, it indicates ns.

**Reanalysis of the data of previous longitudinal *in vivo* imaging**

We reanalyzed the P4 *in vivo* imaging data of OBIs from our previous study (Nakazawa et al., 2018). We compared the OBI difference of L4 neurons at $P4_M$ (noon) and $P4_L$ (8 PM) since that time window fits with the time at which we performed *in vivo* imaging in the current study (1 PM to 9 PM at P4). We also analyzed the OBI differences between SS and SP neurons at P4 (the average OBI of $P4_M$ and $P4_L$). See Table 2.

**Results:**

***In vivo* imaging of developing dendrites with improved spatiotemporal resolution**

To visualize the dendritic morphology of neonatal cortical neurons *in vivo*, we used the *in utero* electroporation (IUE)-based Supernova system (Luo et al., 2016; Mizuno et al., 2014), which labels cortical neurons sparsely and brightly for improved signal to background (Figures 1A, 1B). As a fluorescent label, in our previous studies we employed regular RFP (cytosolic RFP, cRFP) (Mizuno et al., 2014; Nakazawa et al., 2018), but the much stronger fluorescence in the cell body than dendrites (Figure 1C) necessitated multiple tracings of the same dendrite at different image contrast settings for complete and accurate reconstruction. To solve this problem and facilitate faster dendrite reconstruction, in the current study we used membrane-bound RFP (mRFP) (Liu et al., 1994; Moriyoshi et al., 1996), which reduced somal relative to dendrite emission and enabled clearer visualization of dendritic morphologies *in vivo* (Figure 1D). This enhanced accuracy and efficiency even enabled detailed detection of dendritic tips, including growth cone-like and filopodium-like structures (Figures 1D'−1D'''), which were subsequently confirmed by *post hoc* high-magnification confocal imaging in brain slices (Figures 1E−1E''').

To visualize the barrel map, we used TCA-GFP Tg mice (Mizuno et al., 2014). We labeled L4 neurons in the barrel cortex of these mice with the IUE-based Supernova-mRFP. We then performed craniotomy at P4 (morning) and conducted hourly time-lapse imaging for a total of 8 h [or 9 imaging sessions, hour 0 (h0) to h8, Figures 2A, 2B]. Brain samples were then collected for *post hoc* histological analysis (Figure 2C). For quantitative analysis of dendritic dynamics, we considered only L4 neurons located on barrel edges with clear basal dendritic patterns for all 9 imaging sessions (see Materials and Methods). Tangential views of an example neuron from h0 to h8 sessions and *post hoc* histological imaging are shown in Figures 2D and 2E, respectively. In total, we obtained dendritic images from 19 neurons (Table 1) in three mice satisfying these criteria.

This improved spatiotemporal resolution revealed rapid changes in dendrite morphology, including the emergence (*e.g.*, Figures 3A, 3C, 3D) and elimination (*e.g.*, Figures 3B, 3C, 3D) of dendritic trees and branches between two consecutive imaging sessions. These rapid dendrite dynamics detected with hourly imaging were difficult to detect using our previous 8-h interval imaging strategy. For example, in the case of Figure 3C, a dendritic branch that emerged between the first and second (h0 and h1) sessions disappeared between the h2 and h3 sessions. This kind of transient branches were likely missed by our previous 8-h-interval imaging. In the case of Figure 3D, after a branch was eliminated between the h1 and h2 sessions, another branch emerged at a similar position between h2 and h3 sessions. It is highly likely that these two branches at similar locations were recognized as the same branch by lower time-resolution imaging (Figure 3D'). Thus, the high-spatiotemporal resolution achieved using mRFP and shorter acquisition interval in the current study allowed us to conduct more comprehensive mechanistic analyses.

**Three-dimension (3D) reconstruction of L4 neuron dendritic patterns.**

To reveal the detailed dendritic dynamics of barrel cortex L4 neurons at P4, we reconstructed the 3D morphology of all dendrites (basal and apical dendrites) from 19 neurons (the example neuron in Figure 4 is the same neuron as shown in Figure 2D). After tracing and reconstructing dendritic patterns of the same neuron from the 9 imaging sessions, we simplified the temporal patterns by drawing schematics for more efficient evaluation of morphological changes (Figure 4).

We identified the same dendritic trees, which are extensions originating from the cell body, across imaging sessions by comparing morphologies in the 3D view (Figure 4A). Then, tree IDs (tr X) were assigned to the individual basal dendritic trees of each neuron (Figure 4B). The same trees from each imaging session were arranged in the same rows in the schematics (left to right, h0 to h8 imaging sessions). The same "dendritic segments" (see Materials and Methods) were also identified from different imaging sessions and placed at the same angles. We then classified individual dendritic segments into barrel-inner and -outer according to location as previously described (Nakazawa et al., 2018). Inner and outer dendritic segments accounted for all or the majority of segments belonging to the barrel-inner and outer half, respectively. If a dendritic tree extends along the barrel border, it is possible that it includes both inner and outer dendritic segments (*e.g.*, tr 3 in Figure 4B).

By comparing the same dendritic trees and dendritic segments in schematics, we were able to easily identify newly emerged (arrowheads in schematics) and eliminated dendritic trees and branches. These schematics were useful for characterizing detailed changes in dendritic patterns during the 8 h of *in vivo* imaging.

**Basal dendritic dynamics of L4 neurons in neonatal barrel cortex.**

We first analyzed the general properties of dendritic tree dynamics *in vivo*. The total number of basal dendritic trees per neuron was rather stable during the 8 h of imaging (Figure 5A). To

investigate dynamics of L4 neuron dendritic trees systematically, we quantified emerged, eliminated and transiently appearing (emerged and then eliminated within 8 h) trees across the 9 imaging sessions. In the temporal window, 3.32 ± 0.45 trees emerged and 3.32 ± 0.46 were eliminated. Notably, a substantial number (1.68 ± 0.28) were transient (Figure 5B). Further, newly emerged trees were often short lived, and about 20% (6 out of 33) disappeared by the next imaging session (Figure 5C), underscoring the importance of the improved temporal resolution.

Next, we analyzed dendritic tip dynamics of L4 neurons. The total number of basal dendritic tips from each neuron did not change substantially over 8 h (Figure 5D). We then normalized the numbers of basal dendritic tips that emerged, were eliminated, or appeared transiently in 8 h by the total basal dendritic length (see Materials and Methods) and again found similar densities of emergence and elimination (34.62 ± 5.01 vs. 32.44 ± 3.73 per mm) over 8 h (Figure 5E). There were 21.50 ± 3.00 (per mm) transient tips and about half (109 out of 214) of the newly emerged tips disappeared by the next imaging session (Figure 5F).

We then grouped basal dendritic tips into three categories, retraction (R: shortened more than 3 µm), elongation (E: extended longer than 3 µm), and stable (S: length changes less than 3 µm) (see Materials and Methods). Roughly 28% of tips retracted during the time window, 28% elongated, and 43% were stable (Figure 5G). An important parameter of dendritic dynamics is how often dendritic tips switch between E and R behavior. We quantified these events for two consecutive imaging sessions as follows. When a tip continued to elongate across two consecutive sessions, it was categorized as “Elongation-Elongation (EE)”, and when a tip became shorter across two consecutive hours it was categorized as “Retraction-Retraction (RR)”. Further, when a tip was elongated at one measurement time and shorter at the next, it was categorized as “Elongation-Retraction (ER)” and vice versa. The overall frequency of switching events (ER & RE) was higher than the frequency of stability (EE & RR) over two consecutive sessions (Figure 5H). This result further highlights the highly dynamic nature of L4 neuron basal dendrites at P4.

**Comparison of short-term dynamics between the inner and outer basal dendrites.**

Although L4 neurons in barrel cortex have both inner and outer basal dendrites, these neurons receive inputs primarily onto inner basal dendrites because TCAs densely innervate the barrel center but not the septa (Figure 2C). Dendritic refinement largely relies on TCA inputs (Harris & Woolsey, 1981; Li et al., 2013; Mizuno et al., 2018; Nakazawa et al., 2018; Nakazawa et al., 2020; Narboux-Nême et al., 2012), so the spatial bias of TCA inputs may drive dendritic dynamics. The numbers of inner dendritic trees and tips did not change markedly during 8 h of imaging (Figures 6A, 6B). Similarly, the number of outer dendritic trees and tips did not change substantially (Figures 6A, 6B). Moreover, the numbers of newly emerged, eliminated, and transient trees were similar between the inner and outer of barrels over 8 h (Figure 6C). The numbers of dendritic tips (per total inner or outer dendritic length) that emerged, were eliminated, and transiently appeared within 8 h did not differ significantly between inner and outer dendritic fields (Figure 6D). Furthermore, the change in tip length across two consecutive imaging sessions was also similar between inner and outer fields (Figure 6E). Thus, basal dendritic trees and tips demonstrated comparable short-term dynamics between inner and outer dendrites of barrel cortex L4 neurons at P4.

In the mouse barrel cortex L4, excitatory neurons are classified as SS or star pyramid (SP) neurons. Our IUE-based Supernova labels both types of neurons, although the majority of labeled neurons are of the SS type (Nakazawa et al., 2018). The barrel center-oriented asymmetric basal dendritic pattern is a characteristic of SS neurons but not SP neurons, suggesting potential differences in short-term dynamics between inner and outer basal dendrites, especially those of SS neurons. In the adult brain, SP neurons are distinguished by the presence of apical dendrites, which are lacking in SS neurons (Scala et al., 2019; Staiger et al., 2004). On the other hand, the majority of SS neurons at P4 still have the apical dendrite (Callaway & Borrell,

2011; Nakazawa et al., 2018) and thus are difficult to distinguish from SP neurons. However, our previous longitudinal *in vivo* imaging study conducted between P3 and P6 revealed that SS neurons exhibit a higher orientation bias index (OBI, see Materials and Methods) than SP neurons even before the initiation of apical dendrite retraction (Nakazawa et al., 2018). Therefore, we here re-evaluated all imaged neurons (14 SS and 7 SP neurons) in our previous longitudinal imaging study and found that OBIs were significantly higher in SS than SP neurons at P4 [0.417−0.858 (median = 0.730) vs 0.416−0.580 (median = 0.473)] ($p = 0.006$, Mann-Whitney test) (Table 2). Based on this finding, we selected only neurons with High-OBI (> 0.600: 9 neurons) as prospective SS neurons from 19 neurons that were imaged in the current study (Table 1). Notably, 4 out of 9 High-OBI neurons had no apical dendrite or an extremely short (~30 μm) apical dendrite, which is a characteristic of mature SS neurons. We then compared the dynamics between inner and outer basal dendrites of these High-OBI neurons and found that the numbers of trees and tips of basal dendrites that emerged, disappeared, or were transient were still similar between inner and outer dendrites. Thus, even within the High-OBI neuron group (*i.e.*, prospective SS neurons), there were no differences in the dynamics between inner and outer dendrites (Figures 6F, 6G). Furthermore, the length change in 1 h was also similar between inner and outer tips of High-OBI neurons (Figure 6H).

We also compared basal dendritic dynamics between High- and Low-OBI neurons (defined as lower than 0.500, 8 out of 19 neurons, Table 1), while neurons with intermediate OBIs (0.500−0.600, 2 neurons) were excluded. All Low-OBI neurons had substantially longer apical dendrites, suggesting that these were SP or less mature SS neurons. High-OBI neurons showed fewer newly emerged and transient basal dendritic trees, compared with Low-OBI neurons (Figure 7A). A similar tendency was observed in the number of eliminated dendritic trees, although the difference was not significant ($p = 0.106$). These results indicate that High-OBI neurons produce fewer trees than Low-OBI neurons in a short time window. In other words,

High-OBI neurons were more stable than Low-OBI neurons. We next compared the dynamics of basal dendritic tips between High- and Low-OBI neurons. There were fewer emergent and transient dendritic tips (per mm) among High-OBI neurons compared to Low-OBI neurons (Figure 7B). The number of eliminated dendritic tips also showed a similar tendency for lower dynamics, although the difference was not significant ($p = 0.059$). It is likely that both of prospective SP and less mature SS neurons are categorized as Low-OBI neurons at P4. In fact, in the re-evaluation of our previous longitudinal imaging data, 1 out of 14 SS neurons and 5 out of 7 SP neurons showed low OBI ($< 0.500$) at P4. Thus, these results from the current imaging may suggest that mature SS neurons have less dynamic basal dendrites than SP and less mature SS neurons.

In addition to these quantitative analyses, we also carefully examined the behavior of individual basal dendritic trees located around barrel edges in High-OBI neurons, including whether the growth direction of dendritic tips is re-oriented from outward to inward at the barrel edge and if basal dendrites form more branches inward than outward. Examination of all basal dendritic trees (43 trees from 9 High-OBI neurons) expanded around the barrel edges revealed neither reorientation at the barrel edge nor more frequent inward orientation (see example in Figure 7C). There were no detectable differences in dynamics or turning direction between inner and outer tips. Both inner and outer tips demonstrated similar behaviors such as retraction, elongation, elimination, and emergence. These results suggest that basal dendritic asymmetry is generated not through directed outgrowth or reorientation of dendrites but through trial-and-error emergence, elongation, elimination, and retraction of dendritic branches and trees.

**The tip features of basal dendrites are correlated with behavior.**

Taking advantage of the high spatiotemporal resolution of our *in vivo* imaging system, we examined if basal dendrite tip thickness represents its behavior. Indeed, elongating dendritic tips were often thicker (red arrow in Figure 8A), while retracting tips were often thinner (red arrow in Figure 8B). We analyzed these associations quantitatively by calculating correlations. For this analysis, we considered only dendritic tips with clear morphology and measured the mRFP signal intensity in the tip (T) and shaft (S) parts to calculate a "tip thickness index" (TTI) by dividing T by S (examples as in Figure 8C, also see Materials and Methods). We found that TTI was positively correlated with tip-segment length changes in 2 h (between 1 h before and 1 h after the tip thickness quantification) (Figure 8D). In other words, dendritic tips with smaller TTIs, which showed thinner tips in morphology, tended to be retracting while thicker tips with larger TTIs tended to be elongating. We also found that the continuously elongating (EE) tips in two consecutive hours had significantly larger TTIs than those of continuously retracting (RR) tips at the middle time point of extension or retraction (Figure 8E).

In *Drosophila* larvae, dendritic pruning of C4da sensory neurons is mediated by severing and degeneration, in which the proximal part of a dendrite is severed and subsequently the parts of dendrites that are distal from the severed point are degenerated and disappeared (Jan & Jan, 2010; Kanamori et al., 2013; Kuo et al., 2005). To examine whether a similar severing/degeneration mechanism is involved in basal dendrite retraction of mouse neonatal cortical neurons, we focused on dendritic tips that were retracted between h7 and h8 sessions. We carefully observed both *in vivo* images of neurons at the h8 session and high magnification confocal images of the same neurons in the *post hoc* fixed brain slices and examined whether there are debris-like structures at sites where the dendritic tip disappeared between the h7 and h8 sessions. No such debris-like structures were found in 41 instances of late tip disappearance (including 10 cases from the outer basal dendrites of High-OBI neurons) (examples as in Figure

9). Thus, we found no evidence for the possibility that dendritic retraction in barrel cortex L4 neurons involves dendrite severing and degradation.

**Discussion:**

**Short-term dynamics of dendrites in the neocortex during developmental refinement.**

In the current study, we analyzed the short-term dendritic dynamics of L4 neurons in the mouse barrel cortex during neonatal development. *In vivo* imaging at 1-h interval allowed us to precisely identify the same dendritic trees and branches across imaging sessions (Figures 2–4), which were often difficult in previous 8-h interval imaging (Nakazawa et al., 2018). In addition to greater temporal resolution, this study used a membrane-bound RFP, which enabled the precise visualization of dendrite morphology *in vivo* without laborious contrast adjustments (Figure 1). These improvements in spatiotemporal resolution allowed us to detect detailed morphological changes at the level of "individual" dendritic trees and branches in the neonatal cortex (Figures 3 and 4). We found that many dendritic trees and branches (tip-segments) emerged and were eliminated within 8 h (Figures 5A–5F). In addition, dendritic tips often changed direction from elongation to retraction or from retraction to elongation between two consecutive imaging sessions (Figures 5G, 5H). Thus, basal dendrites of barrel cortex L4 neurons are highly dynamic during the refinement period in neonatal development.

Traditional studies of dendrite dynamics in the developing mammalian brain have used *in vitro* systems such as pyramidal neurons in acute slices of the mouse neocortex or cultured cerebellar Purkinje cells of the mouse (Fujishima et al., 2012; Jontes & Smith, 2000; Portera-Cailliau et al., 2003). *In vivo* studies mostly used optic tectal neurons of *Xenopus* tadpole and zebrafish larvae, whose brains are transparent, and focused primarily on how dendrites arborize

(Nagel et al., 2015; Niell et al., 2004; Rajan et al., 1999; Sanchez et al., 2006; Sin et al., 2002; Wu & Cline, 1998; Wu et al., 1999). The optic tectal neuron has a single dendrite. In contrast, SS neurons, the major type of L4 glutamatergic neurons (65%–80% of the total) (Fox, 2008), in the mouse barrel cortex have multiple basal dendrites that exhibit an asymmetric pattern strongly oriented toward the barrel center in adulthood, which is the basis of the precise one-to-one relationship between individual whisker stimulation and barrel activation (Lübke et al., 2000; Staiger et al., 2004). Therefore, it is particularly important to determine how the asymmetric dendritic patterns of SS neurons are generated.

It is generally assumed that SS neuron dendrites show symmetric patterns in early neonatal stages and are refined to acquire asymmetric patterns by simply eliminating outer dendrites and adding new inner dendrites and/or elaborating existing inner dendrites during later neonatal stages (Emoto, 2011; Espinosa et al., 2009; Greenough & Chang, 1988; Iwasato, 2020). We have challenged this conventional view by developing *in vivo* imaging approaches for the neonatal mouse cortex to analyze dynamic processes of SS neuron dendritic refinement (Iwasato, 2020). As a first step, we previously conducted *in vivo* imaging of L4 neuron dendrites starting at P5 (9-h interval for 18 h) (Mizuno et al., 2014), which provides the first observation of dendritic motility in the mammalian brain *in vivo*. This study revealed that branches of inner dendrites are not only elongated but also often retracted. Similarly, branches of outer dendrites show both elongation and retraction. Our recent longitudinal *in vivo* imaging of L4 neurons in the mouse barrel cortex revealed that SS neurons establish basal dendritic orientation bias through two phases (Nakazawa et al., 2018). During Phase I (by P3), SS neurons produce a larger number of inner basal dendritic trees than outer trees, although both inner and outer trees are similarly primitive in morphology at P3. During Phase II (between P3 and P6), the ratio of inner to outer trees does not change. But individual dendritic trees show extensive turnover. Both inner and outer dendritic trees often disappear quickly. Meanwhile, only a few trees highly elaborate. These

510 "winner" trees emerged specifically from inner trees, which generates a strong orientation bias of
511 SS neuron basal dendrites. Although that study revealed the long-term dynamics that generate
512 orientation bias, the spatiotemporal resolution was not sufficient to capture short-term dynamics.
513 In that study, to cover the whole refinement processes between P3 and P6, we set acquisition
514 intervals of 8 or 24 hours. However, the changes in dendrite morphology over 8 h are larger than
515 we initially expected, which hindered the detection of rapid changes over shorter periods. For
516 example, temporal resolutions of these studies were not high enough to quantitatively analyze the
517 frequency of emergence and elimination of dendritic branches.

518 In the current study, we focused on P4, which is the peak time of Phase II (Nakazawa et
519 al., 2018), and asked whether there were differences in short-term dynamics between inner and
520 outer basal dendrites. On the other hand, at this age, it is often difficult to distinguish SS and SP
521 neurons because many SS neurons still have apical dendrites (Nakazawa et al., 2018). Therefore,
522 we also compared dynamics between inner and outer basal dendrites of High-OBI neurons by
523 assuming that the majority of these neurons is prospective SS neurons (see Results for the detail).
524 In either of all-L4-excitatory-neuron population or High-OBI neuron population, both inner and
525 outer trees emerged and were eliminated with no marked difference in frequency (Figure 6).
526 Similarly, inner and outer branches showed comparable frequencies of emergence and
527 elimination and similar behaviors of elongation and retraction (Figure 6). Thus, although basal
528 dendritic trees and branches of SS neurons were highly dynamic during Phase II, rapid changes in
529 basal dendritic structure did not directly contribute to the formation of asymmetric basal dendritic
530 patterns of SS neurons. Taken all the data from our current and previous *in vivo* imaging studies
531 together, we propose that SS neurons establish highly asymmetric dendritic patterns through
532 extensive trial-and-error emergence, elongation, elimination, and retraction of dendritic trees and
533 branches rather than simple emergence/elongation of inner dendrites and elimination/retraction of
534 outer dendrites.

In the current study, we also found that the basal dendritic trees and tips of High-OBI (> 0.600) neurons were less dynamic (*i.e.*, exhibited fewer emergent and transient events over the 8-h imaging period) compared to Low-OBI (< 0.500) neurons (Figures 7A, 7B). It is likely that the majority of High-OBI neurons are of the SS type while Low-OBI neurons may include SP neurons and less mature SS neurons (See Results for the detail). Our previous study shows that dendritic dynamics at P5 are increased in the absence of *N*-Methyl-D-aspartic acid (NMDA) receptor activity (Mizuno et al., 2014). Because NMDA receptor is a key player in dendritic refinement (Datwani et al., 2002; Espinosa et al., 2009; Mizuno et al., 2014), it is possible that dendritic dynamics are reduced with the progress of dendritic refinement.

A caveat of our short-interval imaging is possible effects of anesthesia on activity-dependent dendritic refinement. During early postnatal stages, sensory cortices show spontaneous activities characterized by correlated firing that is arranged spatially according to the modality, and this correlated activity is important for neuronal circuit refinement (Nakazawa & Iwasato, 2021). In the neonatal barrel cortex, spontaneous activity shows a barrel-corresponding patchwork-typed spatial pattern, and this activity is blocked by general anesthesia with isoflurane (Mizuno et al., 2018). Patchwork spontaneous activity is detected again in 5~7 minutes after stopping the isoflurane supply and fully recovers within 10 minutes (See Fig. S1D of (Mizuno et al., 2018)). Similarly, spontaneous activity in the neonatal mouse visual cortex is recovered within 10 minutes after stopping isoflurane inhalation (Ackman et al., 2012). In the experiment setting of the current study, we started and stopped isoflurane supply 2 minutes before the start of each imaging session and 2 minutes before the end of the imaging session, respectively. After finishing each imaging session (20 minutes), we confirmed that pups woke up and started to interact with littermates within 5 minutes. Therefore, pups were anesthetized for nearly 30 minutes in one hour between two consecutive imaging sessions. Thus, it is likely that short-term dendritic dynamics of mouse cortical neurons is even faster than what we observed here.

**Specific dendritic features during development revealed by improved spatiotemporal resolution of *in vivo* imaging.**

The high spatiotemporal-resolution imaging achieved in the current study also enabled us to examine correlations between morphological features and dendritic tip dynamics (Figure 8). We found a positive correlation between dendritic tip thickness and its behavior (Figure 8D). Thick tips, which may have dendritic growth cones (Figure 9), were more likely to be extending (Figure 8A) and thin tips were more likely to be retracting (Figure 8B). Conversely, extending and retracting tips are more likely to be thick and thin, respectively (Figure 8E). Similar correlations between dendritic tip morphology and dendrite behavior are observed in optic tectal neurons in *Xenopus* tadpoles (Hossain et al., 2012; Wu & Cline, 1998) and cortical pyramidal neurons in mouse acute slices (Portera-Cailliau et al., 2003). Thus, it is possible to assume dendritic tip behavior based on dendritic tip morphology revealed by two-photon *in vivo* imaging or confocal imaging of fixed brain slices.

As mentioned above, before *in vivo* time-lapse imaging was achieved, it was generally believed that SS neurons initially have radially oriented basal dendrites and during critical period of dendritic refinement these neurons specifically prune the outer dendrites to acquire highly asymmetric dendritic patterns (Emoto, 2011; Mizuno et al., 2014). If so, it could be similar to class IV dendritic arborizing (C4da) sensory neurons in *Drosophila*, which prune their dendritic arbors during the early metamorphosis. In this pruning process, dendrites are severed and fragmented, and fragments are finally cleared by engulfment (Kanamori et al., 2013; Kuo et al., 2005; Williams et al., 2006; Williams & Truman, 2005). It was wondered whether similar mechanisms may be involved in SS neuron dendritic refinement. By taking advantage of high spatiotemporal resolution of the current imaging, we here carefully observed loci where dendritic segments disappeared within the last 1 h (h7 to h8) combined with *post hoc* confocal imaging of

585 the same loci with high magnification. However, we found no evidence of dendrite severing and
586 fragmentation. This result suggests that the outer basal dendritic trees are unlikely to be pruned
587 from SS neurons in a process akin to that observed for *Drosophila* class IV C4da neurons. In
588 accord with this finding, our previous longitudinal imaging study reveals that SS neurons
589 establish a highly oriented basal dendritic pattern between P3 and P6 without selective
590 elimination of outer dendritic trees. In fact, the numbers of both inner and outer basal dendrites do
591 not differ substantially between P3 and P6 (Nakazawa et al., 2018). Rather, SS neurons establish
592 unique basal dendritic patterns highly oriented toward the barrel center through selection and
593 elaboration of a few inner dendritic trees as "winners".

594 In the current study, we focused our analyses on the short-term dynamics of barrel cortex
595 L4 neurons at P4, the time of peak refinement. Taking our current results and previous
596 longitudinal imaging together, we have revealed highly dynamic features of basal dendrites in the
597 early postnatal period. Rapid dendritic dynamics do not directly contribute to the highly
598 asymmetric basal dendritic pattern of L4 neurons. Instead, dendritic refinement progresses
599 through massive trial-and-error emergence, elongation, elimination, and retraction of dendritic
600 tips and trees.

601 **References**


602 Ackman, J. B., Burbridge, T. J., & Crair, M. C. (2012). Retinal waves coordinate patterned
603 activity throughout the developing visual system. *Nature*, *490*(7419), 219-225.
604 https://doi.org/10.1038/nature11529

605 Ako, R., Wakimoto, M., Ebisu, H., Tanno, K., Hira, R., Kasai, H., Matsuzaki, M., & Kawasaki, H.
606 (2011). Simultaneous visualization of multiple neuronal properties with single-cell
607 resolution in the living rodent brain. *Molecular and Cellular Neuroscience*, *48*(3), 246-
608 257. https://doi.org/https://doi.org/10.1016/j.mcn.2011.08.005

609 Callaway, E. M., & Borrell, V. (2011). Developmental Sculpting of Dendritic Morphology of
610 Layer 4 Neurons in Visual Cortex: Influence of Retinal Input. *The Journal of*
611 *Neuroscience*, *31*(20), 7456. https://doi.org/10.1523/JNEUROSCI.5222-10.2011

612 Carrillo, J., Nishiyama, N., & Nishiyama, H. (2013). Dendritic Translocation Establishes the
613 Winner in Cerebellar Climbing Fiber Synapse Elimination. *The Journal of Neuroscience*,
614 *33*(18), 7641. https://doi.org/10.1523/JNEUROSCI.4561-12.2013

615 Chiaramello, A., Neuman, T., Peavy, D. R., & Zuber, M. X. (1996). The GAP-43 Gene Is a
616 Direct Downstream Target of the Basic Helix-Loop-Helix Transcription Factors*.
617 *Journal of Biological Chemistry*, *271*(36), 22035-22043.
618 https://doi.org/https://doi.org/10.1074/jbc.271.36.22035

619 Datwani, A., Iwasato, T., Itohara, S., & Erzurumlu, R. S. (2002). NMDA Receptor-Dependent
620 Pattern Transfer from Afferents to Postsynaptic Cells and Dendritic Differentiation in the
621 Barrel Cortex. *Molecular and Cellular Neuroscience*, *21*(3), 477-492.
622 https://doi.org/https://doi.org/10.1006/mcne.2002.1195

623 Emoto, K. (2011). Dendrite remodeling in development and disease
624 [https://doi.org/10.1111/j.1440-169X.2010.01242.x]. *Development, Growth &*

*Differentiation*, *53*(3), 277-286. https://doi.org/https://doi.org/10.1111/j.1440-169X.2010.01242.x

Espinosa, J. S., Wheeler, D. G., Tsien, R. W., & Luo, L. (2009). Uncoupling Dendrite Growth and Patterning: Single-Cell Knockout Analysis of NMDA Receptor 2B. *Neuron*, *62*(2), 205-217. https://doi.org/https://doi.org/10.1016/j.neuron.2009.03.006

Fox, K. D. (2008). *Barrel cortex*. Cambridge University Press.

Fujishima, K., Horie, R., Mochizuki, A., & Kengaku, M. (2012). Principles of branch dynamics governing shape characteristics of cerebellar Purkinje cell dendrites. *Development*, *139*(18), 3442-3455. https://doi.org/10.1242/dev.081315

Greenough, W. T., & Chang, F.-L. F. (1988). Dendritic pattern formation involves both oriented regression and oriented growth in the barrels of mouse somatosensory cortex. *Developmental Brain Research*, *43*(1), 148-152. https://doi.org/https://doi.org/10.1016/0165-3806(88)90160-5

Haas, J., Park, E.-C., & Seed, B. (1996). Codon usage limitation in the expression of HIV-1 envelope glycoprotein. *Current Biology*, *6*(3), 315-324. https://doi.org/https://doi.org/10.1016/S0960-9822(02)00482-7

Harris, R. M., & Woolsey, T. A. (1981). Dendritic plasticity in mouse barrel cortex following postnatal vibrissa follicle damage [https://doi.org/10.1002/cne.901960302]. *Journal of Comparative Neurology*, *196*(3), 357-376. https://doi.org/https://doi.org/10.1002/cne.901960302

Holtmaat, A., Bonhoeffer, T., Chow, D. K., Chuckowree, J., De Paola, V., Hofer, S. B., Hübener, M., Keck, T., Knott, G., Lee, W.-C. A., Mostany, R., Mrsic-Flogel, T. D., Nedivi, E., Portera-Cailliau, C., Svoboda, K., Trachtenberg, J. T., & Wilbrecht, L. (2009). Long-term, high-resolution imaging in the mouse neocortex through a chronic cranial window. *Nature Protocols*, *4*(8), 1128-1144. https://doi.org/10.1038/nprot.2009.89

650 Holtmaat, A., & Svoboda, K. (2009). Experience-dependent structural synaptic plasticity in the
651 mammalian brain. *Nature Reviews Neuroscience*, *10*(9), 647-658.
652 https://doi.org/10.1038/nrn2699
653 Hossain, S., Sesath Hewapathirane, D., & Haas, K. (2012). Dynamic morphometrics reveals
654 contributions of dendritic growth cones and filopodia to dendritogenesis in the intact and
655 awake embryonic brain [https://doi.org/10.1002/dneu.20959]. *Developmental*
656 *Neurobiology*, *72*(4), 615-627. https://doi.org/https://doi.org/10.1002/dneu.20959
657 Iwasato, T. (2020). In vivo imaging of neural circuit formation in the neonatal mouse barrel
658 cortex [https://doi.org/10.1111/dgd.12693]. *Development, Growth & Differentiation*,
659 *62*(7-8), 476-486. https://doi.org/https://doi.org/10.1111/dgd.12693
660 Jan, Y.-N., & Jan, L. Y. (2010). Branching out: mechanisms of dendritic arborization. *Nature*
661 *Reviews Neuroscience*, *11*(5), 316-328. https://doi.org/10.1038/nrn2836
662 Jontes, J. D., & Smith, S. J. (2000). Filopodia, Spines, and the Generation of Synaptic Diversity.
663 *Neuron*, *27*(1), 11-14. https://doi.org/https://doi.org/10.1016/S0896-6273(00)00003-9
664 Kanamori, T., Kanai, M. I., Dairyo, Y., Yasunaga, K.-i., Morikawa, R. K., & Emoto, K. (2013).
665 Compartmentalized Calcium Transients Trigger Dendrite Pruning in Drosophila Sensory
666 Neurons. *Science*, *340*(6139), 1475-1478. https://doi.org/10.1126/science.1234879
667 Kozak, M. (1987). An analysis of 5'-noncoding sequences from 699 vertebrate messenger RNAs.
668 *Nucleic Acids Research*, *15*(20), 8125-8148. https://doi.org/10.1093/nar/15.20.8125
669 Kuo, C. T., Jan, L. Y., & Jan, Y. N. (2005). Dendrite-specific remodeling of Drosophila sensory
670 neurons requires matrix metalloproteases, ubiquitin-proteasome, and ecdysone signaling.
671 *Proceedings of the National Academy of Sciences*, *102*(42), 15230-15235.
672 https://doi.org/10.1073/pnas.0507393102
673 Lübke, J., Egger, V., Sakmann, B., & Feldmeyer, D. (2000). Columnar Organization of Dendrites
674 and Axons of Single and Synaptically Coupled Excitatory Spiny Neurons in Layer 4 of

675 the Rat Barrel Cortex. *The Journal of Neuroscience*, *20*(14), 5300.
676 https://doi.org/10.1523/JNEUROSCI.20-14-05300.2000
677 Lendvai, B., Stern, E. A., Chen, B., & Svoboda, K. (2000). Experience-dependent plasticity of
678 dendritic spines in the developing rat barrel cortex in vivo. *Nature*, *404*(6780), 876-881.
679 https://doi.org/10.1038/35009107
680 Li, H., Fertuzinhos, S., Mohns, E., Hnasko, Thomas S., Verhage, M., Edwards, R., Sestan, N., &
681 Crair, Michael C. (2013). Laminar and Columnar Development of Barrel Cortex Relies
682 on Thalamocortical Neurotransmission. *Neuron*, *79*(5), 970-986.
683 https://doi.org/https://doi.org/10.1016/j.neuron.2013.06.043
684 Liu, Y., Fisher, D. A., & Storm, D. R. (1994). Intracellular sorting of neuromodulin (GAP-43)
685 mutants modified in the membrane targeting domain. *The Journal of Neuroscience*,
686 *14*(10), 5807. https://doi.org/10.1523/JNEUROSCI.14-10-05807.1994
687 Luo, W., Mizuno, H., Iwata, R., Nakazawa, S., Yasuda, K., Itohara, S., & Iwasato, T. (2016).
688 Supernova: A Versatile Vector System for Single-Cell Labeling and Gene Function
689 Studies in vivo. *Scientific Reports*, *6*(1), 35747. https://doi.org/10.1038/srep35747
690 Mizuno, H., Ikezoe, K., Nakazawa, S., Sato, T., Kitamura, K., & Iwasato, T. (2018). Patchwork-
691 Type Spontaneous Activity in Neonatal Barrel Cortex Layer 4 Transmitted via
692 Thalamocortical Projections. *Cell Reports*, *22*(1), 123-135.
693 https://doi.org/https://doi.org/10.1016/j.celrep.2017.12.012
694 Mizuno, H., Luo, W., Tarusawa, E., Saito, Yoshikazu M., Sato, T., Yoshimura, Y., Itohara, S., &
695 Iwasato, T. (2014). NMDAR-Regulated Dynamics of Layer 4 Neuronal Dendrites during
696 Thalamocortical Reorganization in Neonates. *Neuron*, *82*(2), 365-379.
697 https://doi.org/https://doi.org/10.1016/j.neuron.2014.02.026
698 Moriyoshi, K., Richards, L. J., Akazawa, C., O'Leary, D. D. M., & Nakanishi, S. (1996). Labeling
699 Neural Cells Using Adenoviral Gene Transfer of Membrane-Targeted GFP. *Neuron*,
700 *16*(2), 255-260. https://doi.org/https://doi.org/10.1016/S0896-6273(00)80044-6

Nagel, A. N., Marshak, S., Manitt, C., Santos, R. A., Piercy, M. A., Mortero, S. D., Shirkey-Son, N. J., & Cohen-Cory, S. (2015). Netrin-1 directs dendritic growth and connectivity of vertebrate central neurons in vivo. *Neural Development*, *10*(1), 14. https://doi.org/10.1186/s13064-015-0041-y

Nakazawa, S., & Iwasato, T. (2021). Spatial organization and transitions of spontaneous neuronal activities in the developing sensory cortex [https://doi.org/10.1111/dgd.12739]. *Development, Growth & Differentiation*, *63*(6), 323-339. https://doi.org/https://doi.org/10.1111/dgd.12739

Nakazawa, S., Mizuno, H., & Iwasato, T. (2018). Differential dynamics of cortical neuron dendritic trees revealed by long-term in vivo imaging in neonates. *Nature Communications*, *9*(1), 3106. https://doi.org/10.1038/s41467-018-05563-0

Nakazawa, S., Yoshimura, Y., Takagi, M., Mizuno, H., & Iwasato, T. (2020). Developmental Phase Transitions in Spatial Organization of Spontaneous Activity in Postnatal Barrel Cortex Layer 4. *The Journal of Neuroscience*, *40*(40), 7637-7650. https://doi.org/10.1523/jneurosci.1116-20.2020

Narboux-Nême, N., Evrard, A., Ferezou, I., Erzurumlu, R. S., Kaeser, P. S., Lainé, J., Rossier, J., Ropert, N., Südhof, T. C., & Gaspar, P. (2012). Neurotransmitter Release at the Thalamocortical Synapse Instructs Barrel Formation But Not Axon Patterning in the Somatosensory Cortex. *The Journal of Neuroscience*, *32*(18), 6183. https://doi.org/10.1523/JNEUROSCI.0343-12.2012

Niell, C. M., Meyer, M. P., & Smith, S. J. (2004). In vivo imaging of synapse formation on a growing dendritic arbor. *Nature Neuroscience*, *7*(3), 254-260. https://doi.org/10.1038/nn1191

Portera-Cailliau, C., Pan, D. T., & Yuste, R. (2003). Activity-Regulated Dynamic Behavior of Early Dendritic Protrusions: Evidence for Different Types of Dendritic Filopodia. *The*

*Journal of Neuroscience*, *23*(18), 7129. https://doi.org/10.1523/JNEUROSCI.23-18-07129.2003

Portera-Cailliau, C., Weimer, R. M., De Paola, V., Caroni, P., & Svoboda, K. (2005). Diverse Modes of Axon Elaboration in the Developing Neocortex. *PLoS Biology*, *3*(8), e272. https://doi.org/10.1371/journal.pbio.0030272

Rajan, I., Witte, S., & Cline, H. T. (1999). NMDA receptor activity stabilizes presynaptic retinotectal axons and postsynaptic optic tectal cell dendrites in vivo. *Journal of Neurobiology*, *38*(3), 357-368. https://doi.org/https://doi.org/10.1002/(SICI)1097-4695(19990215)38:3<357::AID-NEU5>3.0.CO;2-#

Ruthazer, E. S., Akerman, C. J., & Cline, H. T. (2003). Control of Axon Branch Dynamics by Correlated Activity in Vivo. *Science*, *301*(5629), 66-70. https://doi.org/10.1126/science.1082545

Sanchez, A. L., Matthews, B. J., Meynard, M. M., Hu, B., Javed, S., & Cohen-Cory, S. (2006). BDNF increases synapse density in dendrites of developing tectal neurons in vivo. *Development*, *133*(13), 2477-2486. https://doi.org/10.1242/dev.02409

Scala, F., Kobak, D., Shan, S., Bernaerts, Y., Laturnus, S., Cadwell, C. R., Hartmanis, L., Froudarakis, E., Castro, J. R., Tan, Z. H., Papadopoulos, S., Patel, S. S., Sandberg, R., Berens, P., Jiang, X., & Tolias, A. S. (2019). Layer 4 of mouse neocortex differs in cell types and circuit organization between sensory areas. *Nature Communications*, *10*(1), 4174. https://doi.org/10.1038/s41467-019-12058-z

Sin, W. C., Haas, K., Ruthazer, E. S., & Cline, H. T. (2002). Dendrite growth increased by visual activity requires NMDA receptor and Rho GTPases. *Nature*, *419*(6906), 475-480. https://doi.org/10.1038/nature00987

Staiger, J. F., Flagmeyer, I., Schubert, D., Zilles, K., Kötter, R., & Luhmann, H. J. (2004). Functional Diversity of Layer IV Spiny Neurons in Rat Somatosensory Cortex:

751 Quantitative Morphology of Electrophysiologically Characterized and Biocytin Labeled
752 Cells. *Cerebral Cortex*, *14*(6), 690-701. https://doi.org/10.1093/cercor/bhh029
753 Williams, D. W., Kondo, S., Krzyzanowska, A., Hiromi, Y., & Truman, J. W. (2006). Local
754 caspase activity directs engulfment of dendrites during pruning. *Nature Neuroscience*,
755 *9*(10), 1234-1236. https://doi.org/10.1038/nn1774
756 Williams, D. W., & Truman, J. W. (2005). Cellular mechanisms of dendrite pruning in
757 Drosophila: insights from in vivo time-lapse of remodeling dendritic arborizing sensory
758 neurons. *Development*, *132*(16), 3631-3642. https://doi.org/10.1242/dev.01928
759 Wu, G.-Y., & Cline, H. T. (1998). Stabilization of Dendritic Arbor Structure in Vivo by CaMKII.
760 *Science*, *279*(5348), 222-226. https://doi.org/10.1126/science.279.5348.222
761 Wu, G. Y., Zou, D. J., Rajan, I., & Cline, H. (1999). Dendritic Dynamics *In Vivo* Change during
762 Neuronal Maturation. *The Journal of Neuroscience*, *19*(11), 4472.
763 https://doi.org/10.1523/JNEUROSCI.19-11-04472.1999
764 Yang, G., Pan, F., & Gan, W.-B. (2009). Stably maintained dendritic spines are associated with
765 lifelong memories. *Nature*, *462*(7275), 920-924. https://doi.org/10.1038/nature08577
766 Young, P., Qiu, L., Wang, D., Zhao, S., Gross, J., & Feng, G. (2008). Single-neuron labeling with
767 inducible Cre-mediated knockout in transgenic mice. *Nature Neuroscience*, *11*(6), 721-
768 728. https://doi.org/10.1038/nn.2118

769

**Figure legends**

**Figure 1: Improvement in the spatial resolution of cortical neuron *in vivo* imaging.**

**(A)** The Supernova membrane-bound RFP (mRFP) vector set (Vector 1 and Vector 2) used for *in utero* electroporation (IUE)-based sparse labeling of barrel cortex layer 4 (L4) neurons. Vector 3 was used to identify mice in which neurons in the barrel field were appropriately labeled before the cranial window surgery because dense BFP labeling by Vector 3, but not Supernova-mRFP, was detectable over the skull.

**(B)** Tangential stacks of Supernova-mRFP-labeled L4 neurons in the thalamocortical axon (TCA)-GFP transgenic (Tg) mouse at postnatal day (P) 4. Left to right, the barrel map visualized with TCA-GFP Tg labeling, Supernova-mRFP-labeled L4 neurons, BFP-labeled L4 neurons, and the merged image. A: anterior; L: lateral. Scale bar: 100 μm.

**(C)** *In vivo* images of an L4 neuron labeled with Supernova-cytosolic RFP (cRFP) at P4 (z-stacked). Scale bar: 50 μm.

**(D)** Tangential stacks of *in vivo* images of a Supernova-mRFP-labeled L4 neuron. Scale bar: 50 μm.

**(D'-D''')** Higher magnification images of the red box regions in (D) showed growth cone-like structures (arrows) and filopodium-like protrusions (arrowheads). Scale bar: 10 μm.

**(E)** Tangential stacks of a high magnification confocal image of the neuron shown in (D). Images were taken by a 63x lens with a 2x zoom. Scale bar: 50 μm.

**(E'-E''')** Higher magnification images of corresponding areas shown in (D'-D'''). The growth cone-like and filopodium-like morphologies were confirmed (arrows and arrowheads, respectively). Scale bar: 10 μm.

**Figure 2: One-hour interval *in vivo* time-lapse imaging of L4 neurons in the neonatal barrel cortex.**

**(A)** Experimental design of time-lapse *in vivo* imaging. TCA-GFP Tg mice were used for visualizing the barrel map. L4 neurons in the TCA-GFP mouse barrel cortex were sparsely labeled with Supernova-mRFP via IUE at embryonic day (E) 14. The cranial window was made at postnatal day (P) 4 morning, and the 1-h-interval *in vivo* imaging started 1 h after the surgery. In every imaging session, the pup for *in vivo* imaging was head-fixed to the imaging stage under a two-photon microscope with light anesthesia. The brain of the *in vivo* imaged mouse was collected after 9 (h0 to h8) imaging sessions, and then fixed. Tangential sections were obtained for *post-hoc* confocal analyses.

**(B)** An example of 1-h-interval *in vivo* imaging of Supernova-mRFP-labeled L4 neurons at P4. Z-stacked images from the top view. Scale bar: 100 μm.

**(C)** The *post-hoc* confocal image (z-stacked) of the tangential section of the same area in (B). The neuron pointed with a yellow arrow in (C) is the same neuron pointed in h8 session of (B). The same neurons were identified by their relative positions with each other and dendritic patterns. The *in vivo* imaged neurons were located on C1−C4 barrels in this example mouse. The sample orientations in (B) and (C) were similar. A, anterior; L, lateral. Scale bar: 100 μm.

**(D)** An example of time-lapse images of dendritic morphologies of an L4 neuron in 8 h of imaging sessions. Top views of an L4 neuron (z-stacked), which was located at the edge of the C1 barrel. Snapshots were taken from the 3D reconstruction software Imaris. The neuron was rotated to the same angle and at the same magnification from 9 imaging sessions. The green line in the h8 imaging session showed the C1 barrel edge. Scale bar: 20 μm.

**(E)** The corresponding confocal image (z-stacked) of the neuron (yellow arrow) shown in (D) at a similar angle and magnification. An example neuron is located at the C1 barrel edge. Scale bar: 20 μm.

**Figure 3: Detection of rapid dendritic dynamics with improved spatiotemporal resolution *in vivo* imaging.**

**(A)** A basal dendritic tree (arrowhead) that newly emerged between h7 (left) and h8 (right) sessions. Snapshot images taken in the Imaris software. Scale bar: 5 μm.

**(B)** A basal dendritic tree that disappeared between h0 (left) and h1 (right) sessions. Snapshot images taken in the Imaris software. Scale bar: 5 μm.

**(C)** A transient basal dendritic branch (arrowheads) emerged between h0 and h1 sessions and disappeared between h2 and h3 sessions. Scale bar: 10 μm.

**(D, D')** After a branch (red arrowheads) was eliminated between h1 and h2 sessions, another branch (yellow arrowheads) emerged at a similar position between h2 and h3 sessions (**D**). It is highly likely that these two branches (red and yellow arrowheads) are recognized as an identical dendrite if only h0 and h5 images are available (**D'**). Snapshot images taken in the Imaris software. Scale bar: 5 μm.

Examples in (A-C) and (D, D') are from Neuron #1 and Neuron #3 (Table 1), respectively.

**Figure 4: Reconstruction of dendritic patterns imaged *in vivo*.**

**(A)** A 2-dimensional view of 3-dimensionally (3D) reconstructed dendritic morphology from the neuron shown in Figure 2D. Representative basal dendritic trees (tr 2 and tr 7) that originated from the barrel-side half (IN) of the cell body and the other half (OUT), respectively, are labeled in red. Scale bars: 20 μm.

**(B)** A schematic that enables simple tracking of dendritic pattern changes during imaging sessions. The representative schematic for the example neuron in (A) is shown. Imaging session numbers (h0 to h8) are shown on the top. The same basal dendritic trees (tr 1−8) were arranged in the same rows in schematics. The same dendritic segments from different imaging sessions were placed at the same angles. Individual dendritic segments were classified into barrel-inner (IN, cyan) and -outer (OUT, magenta) according to their location. The newly emerged inner and outer

branches (and trees) were marked with cyan and magenta arrowheads, respectively. The lengths of individual dendritic trees and segments are roughly proportional. Gray lines, apical dendrite. Scale bar: 20 μm.

**Figure 5: General properties of the dendritic dynamics of L4 neurons at P4.**

**(A)** Changes in basal dendritic tree numbers from each neuron during 8 h of imaging. The gray and black lines represent data of individual neurons and the average, respectively. n = 19 neurons, 3 mice.

**(B)** Numbers of emerged, eliminated, and transient trees from each neuron in 8 h of imaging. The "+" represents the mean value and the horizontal line in the boxplot represents the median. Each dot represents one neuron. n = 19 neurons, 3 mice.

**(C)** Survival ratio of newly emerged trees. In this analysis, only dendritic trees that were first detected at h1, h2, h3, h4, or h5 imaging sessions were used. The imaging session at which the tree was first detected was defined as the time point 0 (n = 33 trees). 27 (81.8%), 19 (57.6%), and 16 (48.5%) of the 33 trees were still present at time points 1, 2, and 3, respectively. n = 16 neurons, 2 mice. 3 out of 19 *in vivo* imaged neurons have no trees that emerged between h1 and h5 sessions.

**(D)** Changes in dendritic tip numbers from each neuron during 8 h of imaging. The gray lines and black lines represent data of individual neurons and the average, respectively. n = 19 neurons, 3 mice.

**(E)** Numbers of emerged, eliminated, and transient tips (per mm) from each neuron in 8 h of imaging. The "+" represents the mean value and the line in the boxplot represents the median. Each dot represents one neuron. n = 19 neurons, 3 mice.

**(F)** Survival ratio of the newly emerged dendritic tips. Only dendritic tips that emerged between h1 to h5 of the *in vivo* imaging sessions were used. At the time point 0, n = 214 tips; 105 (49.1%), 74 (34.6%), and 61 (28.5%) out of 214 dendritic tips were still present at time points 1, 2, and 3,

respectively. n = 19 neurons, 3 mice.

**(G)** Histogram of dendritic tip length changes in 1 h. x-axis shows the length change (μm), and y-axis shows the event number of corresponding length changes. Length changes larger than 3 μm, smaller than -3 μm, and between -3 μm and +3 μm were classified as elongation (E, 28.1%), retraction (R, 28.5%), and stable (S, 43.4%), respectively. n = 2089 dendritic tips (from19 neurons, 3 mice).

**(H)** Frequencies of tip behavior in which individual tips continued to elongate or retract in consecutive 2 imaging sessions (EE&RR) and those of tip behavior in which dendritic tips changed the motility direction from E to R or R to E (ER&RE) were compared. Other behaviors (ES, RS, SE, SR & SS) were excluded from comparison. The "+" represents the mean value and the horizontal line in the boxplot represents the median. Each dot represents one neuron. p = 0.022, Mann-Whitney test. n = 19 neurons, 3 mice.

**Figure 6: Comparison of dynamic properties between the inner and outer dendrites.**

**(A, B)** Changes in the numbers of inner (IN) and outer (OUT) trees (A) and tips (B) from each neuron across 9 imaging sessions. Gray lines represent data for individual neurons. Black lines show the average of all neurons. n = 19 neurons, 3 mice.

**(C)** There were no significant differences between IN and OUT trees in the numbers of emerged, eliminated, and transient trees. p = 0.796, 0.556, 0.234, respectively; Wilcoxon matched-pairs signed rank tests; n = 19 neurons, 3 mice. Red lines represent the average.

**(D)** There were no significant differences between IN and OUT tips in the numbers of emerged, eliminated, and transient tips (per mm basal dendritic length) (p = 0.738, 0.568, and 0.441, respectively; Wilcoxon matched-pairs signed rank tests; n = 19 neurons, 3 mice). The dendritic tip numbers were normalized with the IN or OUT basal dendritic length of the neuron (average length from 9 imaging sessions). Red lines represent the average.

**(E)** There were no significant differences between IN and OUT dendritic tips in 1 h length changes (μm). p = 0.304; Mann-Whitney test; n = 945 IN and 852 OUT tips (from 19 neurons, 3 mice).

**(F)** There were no significant differences between IN and OUT basal dendritic trees of "High-orientation bias index (OBI)" neurons in the numbers of emerged, eliminated, and transient trees. p = 0.648, 0.750, and > 0.999, respectively; Wilcoxon matched-pairs signed rank tests. n= 9 High-OBI neurons, 3 mice. Red lines represent the average.

**(G)** There were no significant differences between IN and OUT dendritic tips of High-OBI neurons in the numbers of emerged, eliminated, and transient tips (per mm IN or OUT basal dendritic length) (p = 0.820, 0.570, and 0.250, respectively; Wilcoxon matched-pairs signed rank tests. n= 9 High-OBI neurons, 3 mice. Red lines represent the average.

**(H)** There were no significant differences between IN and OUT tips of High-OBI neurons in 1 h length changes (μm). p = 0.260; Mann-Whitney test; n = 568 High-IN and 340 High-OUT tips (from 9 High-OBI neurons, 3 mice).

**Figure 7: Comparison of dynamic properties of dendrites between High- and Low-OBI neurons.**

(**A**) Numbers of basal dendritic trees that emerged (p = 0.024), eliminated (p = 0.106), and were transient (p = 0.030) were compared between High- and Low-OBI neurons. The "+" represents the mean value and the horizontal line in the boxplot represents the median. Each dot represents one neuron. Mann-Whitney tests, n = 9 High- and 8 Low-OBI neurons.

**(B)** Numbers of basal dendritic tips that emerged (p = 0.047), eliminated (p = 0.059), and transient (p = 0.036) were compared between High- and Low-OBI neurons. The dendritic tip number was normalized with the total basal dendritic length of the neuron (average length from 9 imaging sessions). The "+" represents the mean value and the horizontal line in the boxplot

represents the median. Each dot represents one neuron. Mann-Whitney tests. n = 9 High- and 8 Low-OBI neurons.

**(C)** Reconstructed dendritic pattern for an example dendritic tree (yellow) from a High-OBI neuron, which is located near the barrel edge (green). An outward basal dendritic tip did not change its direction or start to retract at the barrel edge and elongated outward further (arrow at h8). Two inward tips were generated near the barrel-edge, but both were eliminated immediately (arrowheads at h1 and h6 sessions). Scale bar: 20 μm.

**Figure 8: Dendrite tip features represent their behavior.**

**(A)** An example image of a dendritic branch (tip-segment) whose tip appeared thick at Time 0 (red arrow) was becoming longer and longer between the Time -1 and Time +1 sessions. Red and yellow arrows indicate the distal end of the branch. Snapshot images taken in the Imaris software. Scale bar: 10 μm.

**(B)** An example image of a dendritic branch whose tip appeared thin at Time 0 (red arrow) was becoming shorter and shorter between the Time -1 and Time +1 sessions. Red and yellow arrows indicate the distal end of the branch. Snapshot images taken in the Imaris software. Scale bar: 10 μm.

**(C)** Example diagrams of quantitative analysis for "tip thickness index" (TTI). Left panel: an example for a thin tip, TTI = 0.26. Right panel: an example for a thick tip, TTI = 1.68. The distal part of the tip-segment was divided into 3 units: tip (T), middle, and shaft (S). The length of each unit is 5 μm. Regions of interest (ROIs, the magenta areas) of T and S units were determined according to their morphologies. Snapshot images taken in the Imaris software. Scale bar: 10 μm.

**(D)** Quantification of correlations of TTIs and length changes of tip-segments in 2 h (between Time -1 and Time +1). The x-axis is in $\log_2$ units. $y = 3.689*x - 4.826$. The black curve represents the fitted curve, and the dashed line represents the 95% confidence interval. Each inverted triangle represents individual dendritic tips. n = 79 tips, from 14 neurons, 3 mice.

**(E)** TTIs of tip-segments that continued to extend (EE) were compared with TTIs of tip-segments that continued to retract (RR) in 2 consecutive hours. In this analysis, TTIs were calculated from the middle time points of continuous elongation or retraction. The "+" represents the mean value and the horizontal line in the boxplot represents the median. Each dot represents one neuron. p = 0.003, Mann-Whitney test. n = 5 EE and 7 RR tip-segments, from 5 neurons, 2 mice.

**Figure 9: Observation of loci immediately after dendrite retraction.**

**(A)** Three representative basal dendritic tips retracted between h7 and h8 sessions. The red and yellow arrowheads show positions of basal dendritic tips in h7 and h8 sessions, respectively. Snapshot images taken in the Imaris software. Scale bars: 10 µm.

**(B)** *Post-hoc* (126x) confocal z-stack images corresponding to images in (A). The red and yellow arrowheads show positions of dendritic tips in h7 and h8 sessions, respectively. Brain slices: 100 µm-thick. Scale bars: 10 µm.

**(B')** The higher magnification images of red box areas in (B). Scale bars: 5 µm.

961 **Table 1. Summary of 19 neurons that were used for statistical analyses.**

| Neuron ID | Barrel[a)] | Distance[b)] | OBI[c)] | Type[d)] | AD[e)] | AD length (µm) |
|---|---|---|---|---|---|---|
| #1 | C1 | 12.8 | 0.689 | High | −* | 29.7 |
| #2 | B2 | 10.6 | 0.415 | Low | + | 157.6 |
| #3 | C3 | 2.7 | 0.464 | Low | + | 190.1 |
| #4 | C2 | 9.9 | 0.475 | Low | + | 178.0 |
| #5 | C2 | 0 | 0.386 | Low | + | 486.8 |
| #6 | C4 | 5.8 | 0.747 | High | + | 234.6 |
| #7 | C3 | 2.4 | 0.714 | High | − | 0 |
| #8 | B1 | 11.8 | 0.666 | High | + | 187.4 |
| #9 | B2 | 11.7 | 0.616 | High | + | 189.6 |
| #10 | B4 | 3.3 | 0.545 | Medium | + | 267.1 |
| #11 | C5 | 4.2 | 0.562 | Medium | + | 124.7 |
| #12 | B3 | 9.9 | 0.465 | Low | + | 435.8 |
| #13 | B3 | 19.7 | 0.757 | High | − | 0 |
| #14 | B3 | 2.7 | 0.454 | Low | + | 679.8 |
| #15 | B2 | 16.1 | 0.693 | High | − | 0 |
| #16 | C2 | 1.7 | 0.644 | High | + | 225.7 |
| #17 | B2 | 7.4 | 0.381 | Low | + | 229.8 |
| #18 | C2 | 19.3 | 0.681 | High | + | 447.5 |
| #19 | C2 | 14.0 | 0.367 | Low | + | 207.8 |

962 a) The barrel column which the neuron belongs to.

963 b) The distance (µm) from the center of cell body to the barrel edge.

964 c) Mean OBI (orientation bias index: see Materials and Methods) of 9 imaging sessions of the

965 neuron.

d) High: High-orientation bias index (OBI) neuron, whose OBI was >0.6, Low: Low-OBI neuron, whose OBI was <0.5. Medium: Neurons whose OBI were >0.5 and <0.6 were not included in either High- or Low-OBI groups.

e) AD: apical dendrite. "+" and "–" mean presence and absence of the apical dendrite, respectively. *Note that "Neuron #1" has only an extremely short (~30 μm) apical dendrite.

**Table 2. Reanalysis of neurons that were analyzed in previous longitudinal *in vivo* imaging.**

| Neuron ID | OBI | Neuron type |
|---|---|---|
| #a | 0.712 | SS |
| #b | 0.869 | SS |
| #c | 0.857 | SS |
| #d | 0.808 | SS |
| #e | 0.795 | SS |
| #f | 0.752 | SS |
| #g | 0.747 | SS |
| #h | 0.753 | SS |
| #i | 0.629 | SS |
| #j | 0.575 | SS |
| #k | 0.560 | SS |
| #l | 0.516 | SS |
| #m | 0.503 | SS |
| #n | 0.417 | SS |
| #o | 0.580 | SP |
| #p | 0.563 | SP |
| #q | 0.497 | SP |
| #r | 0.473 | SP |

| | | |
|---|---|---|
| #s | 0.439 | SP |
| #t | 0.430 | SP |
| #u | 0.416 | SP |

973

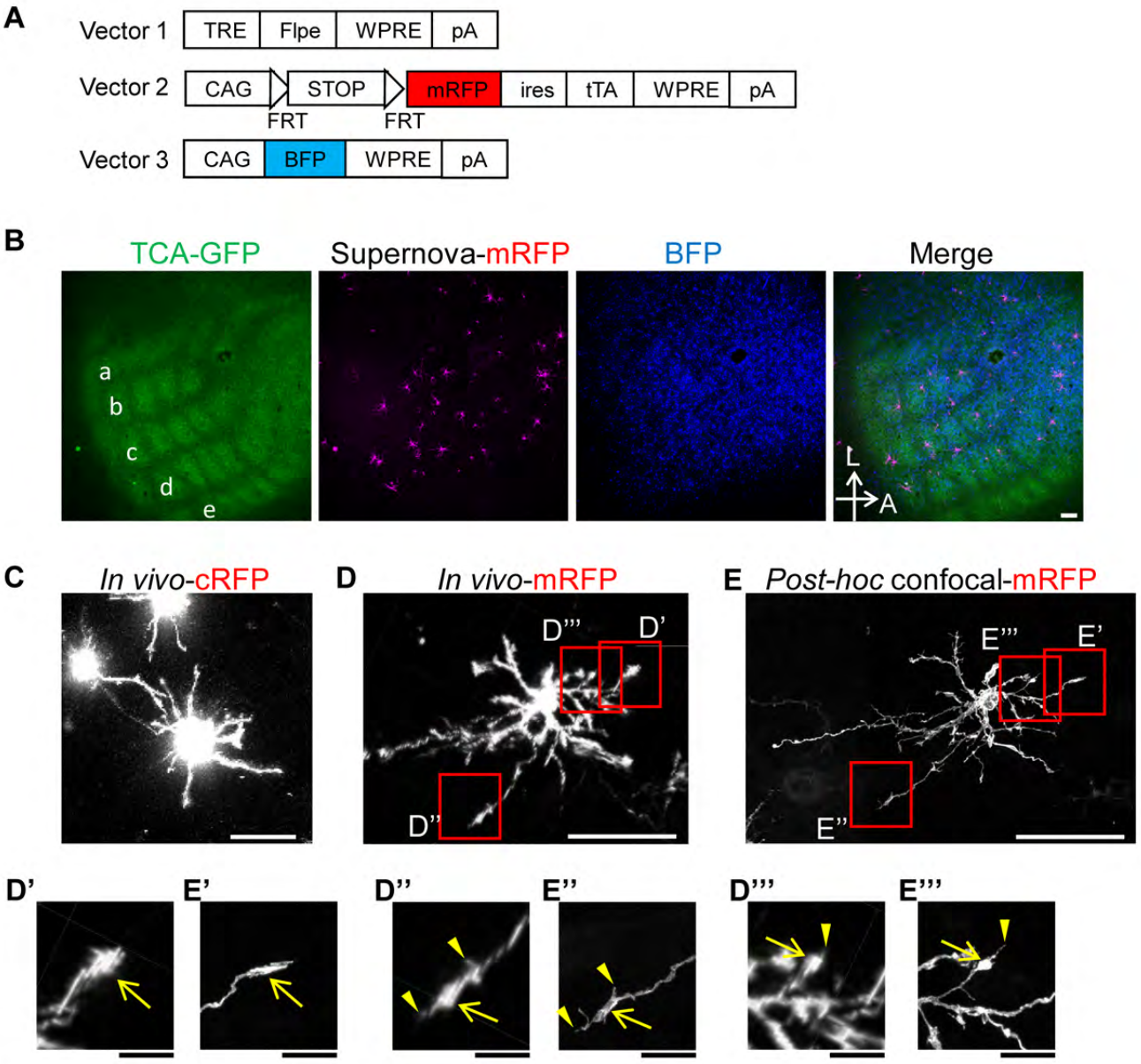


**Figure 1**

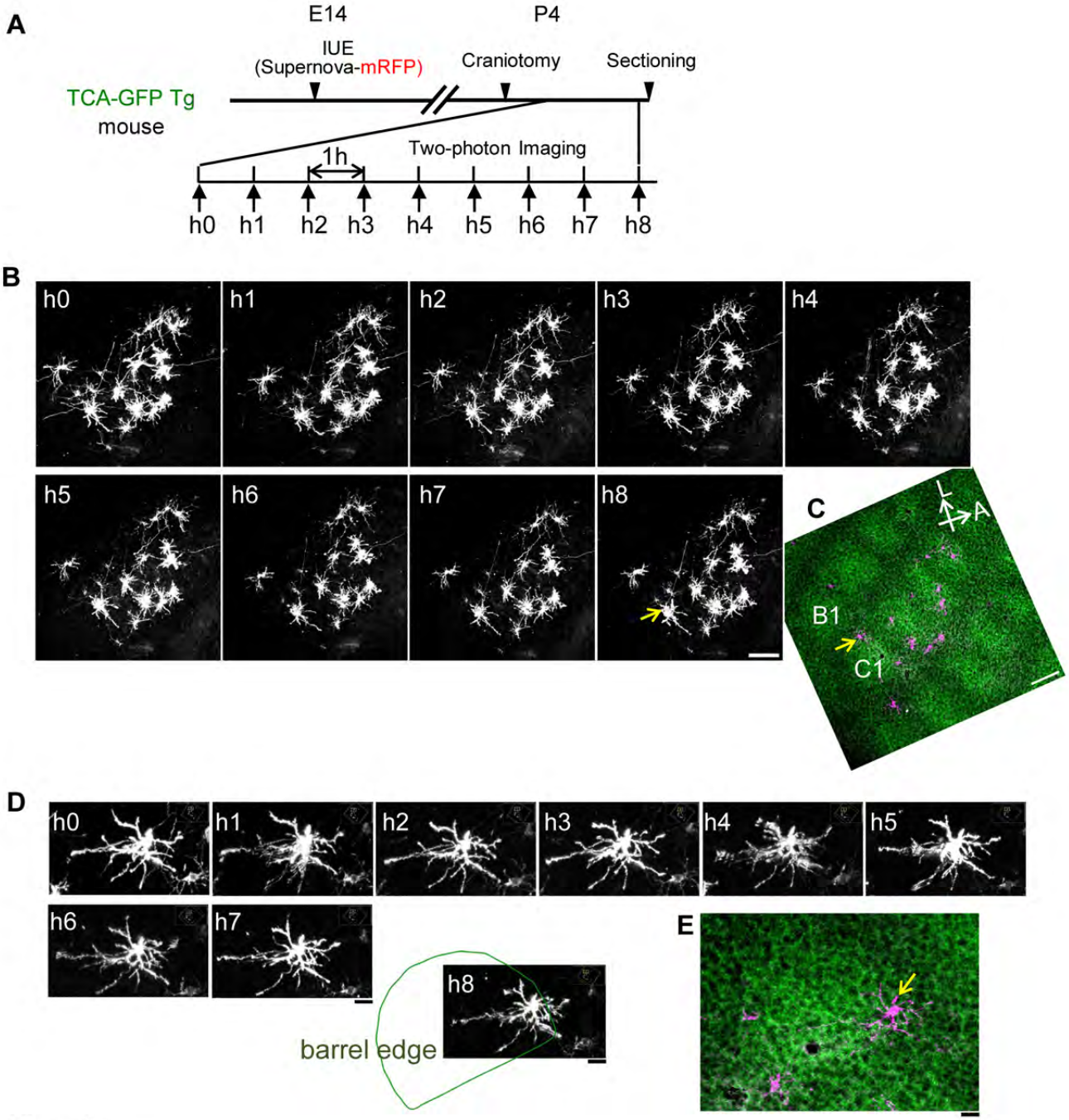


**Figure 2**

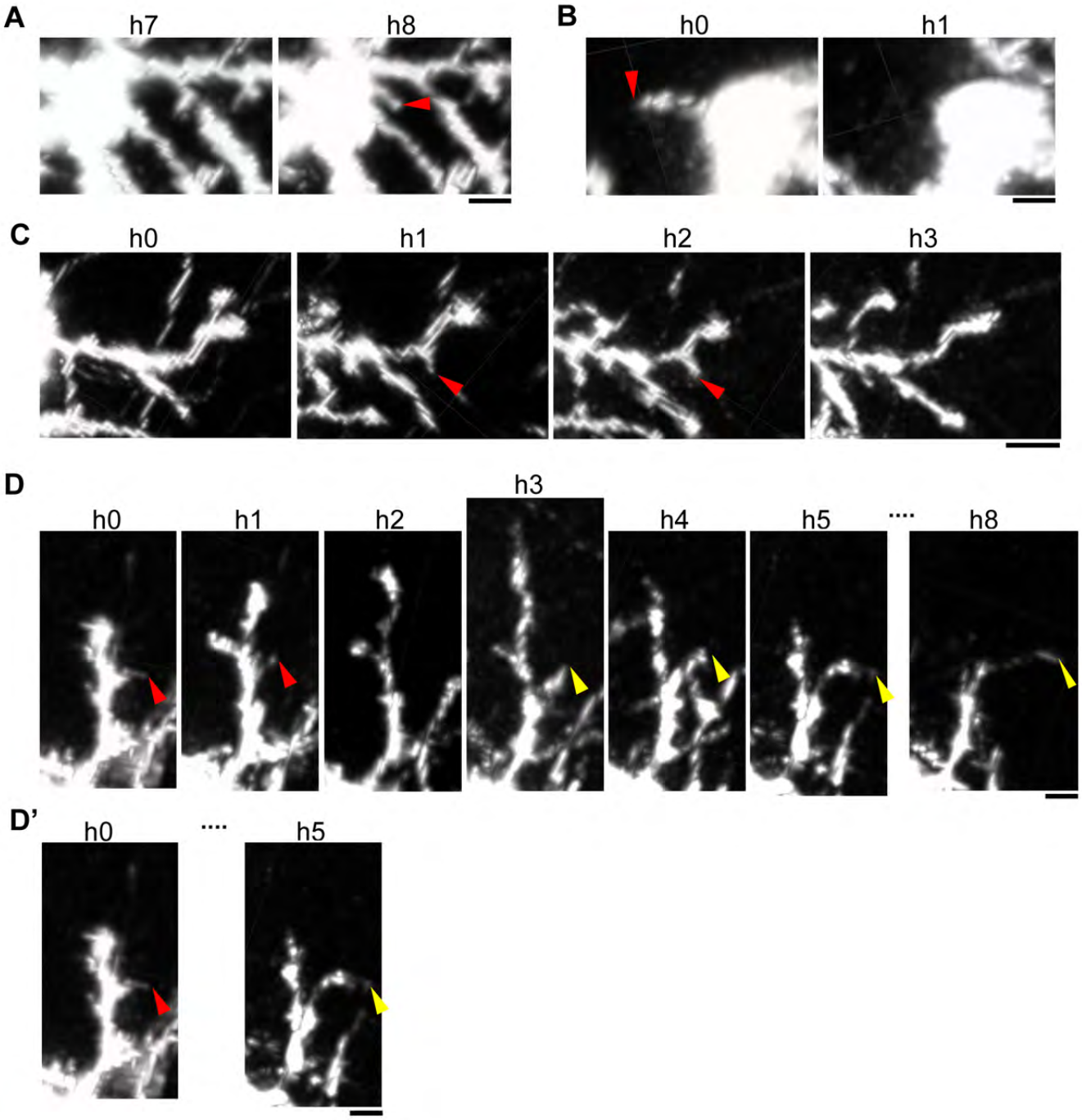


**Figure 3**

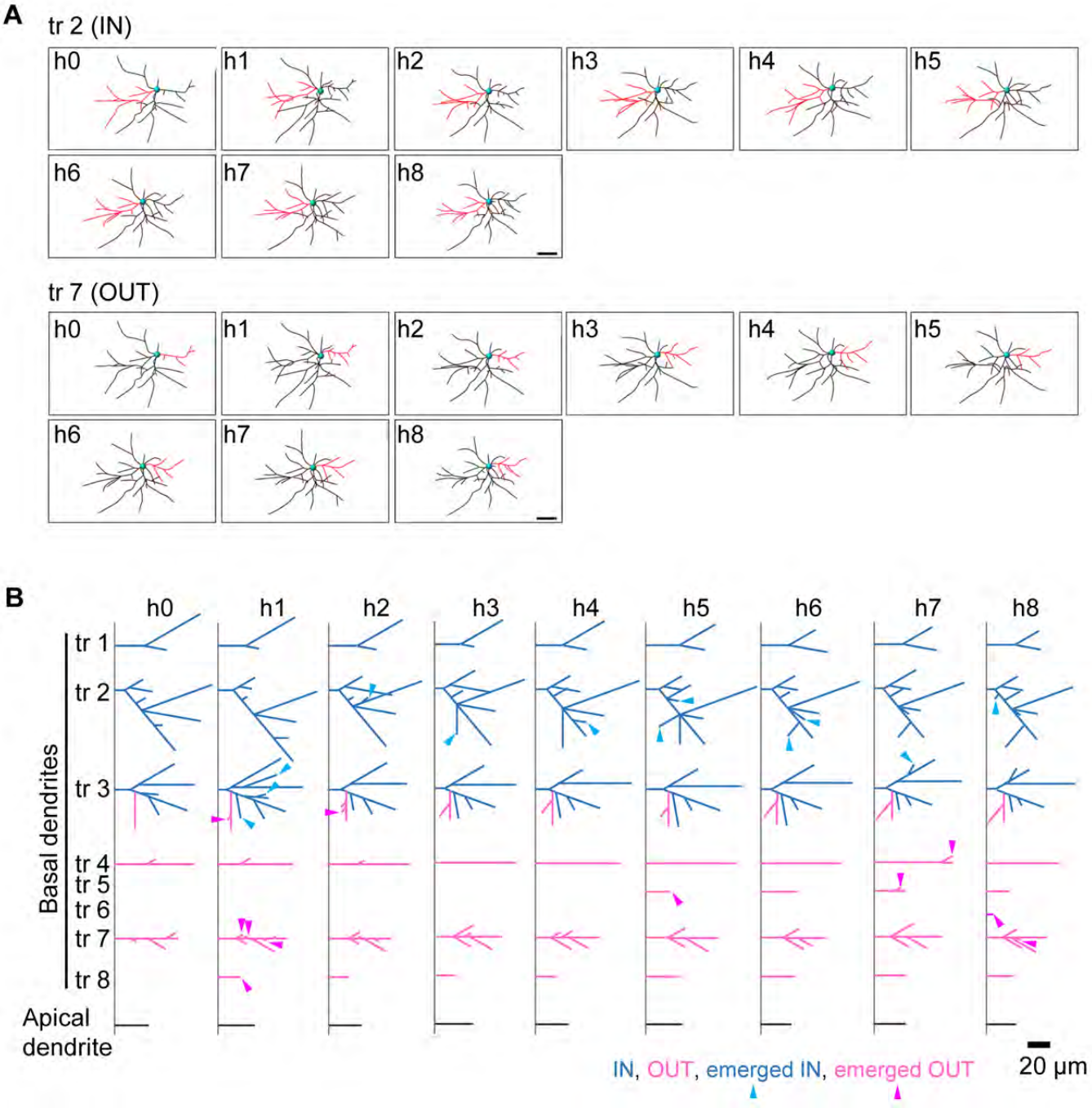


**Figure 4**

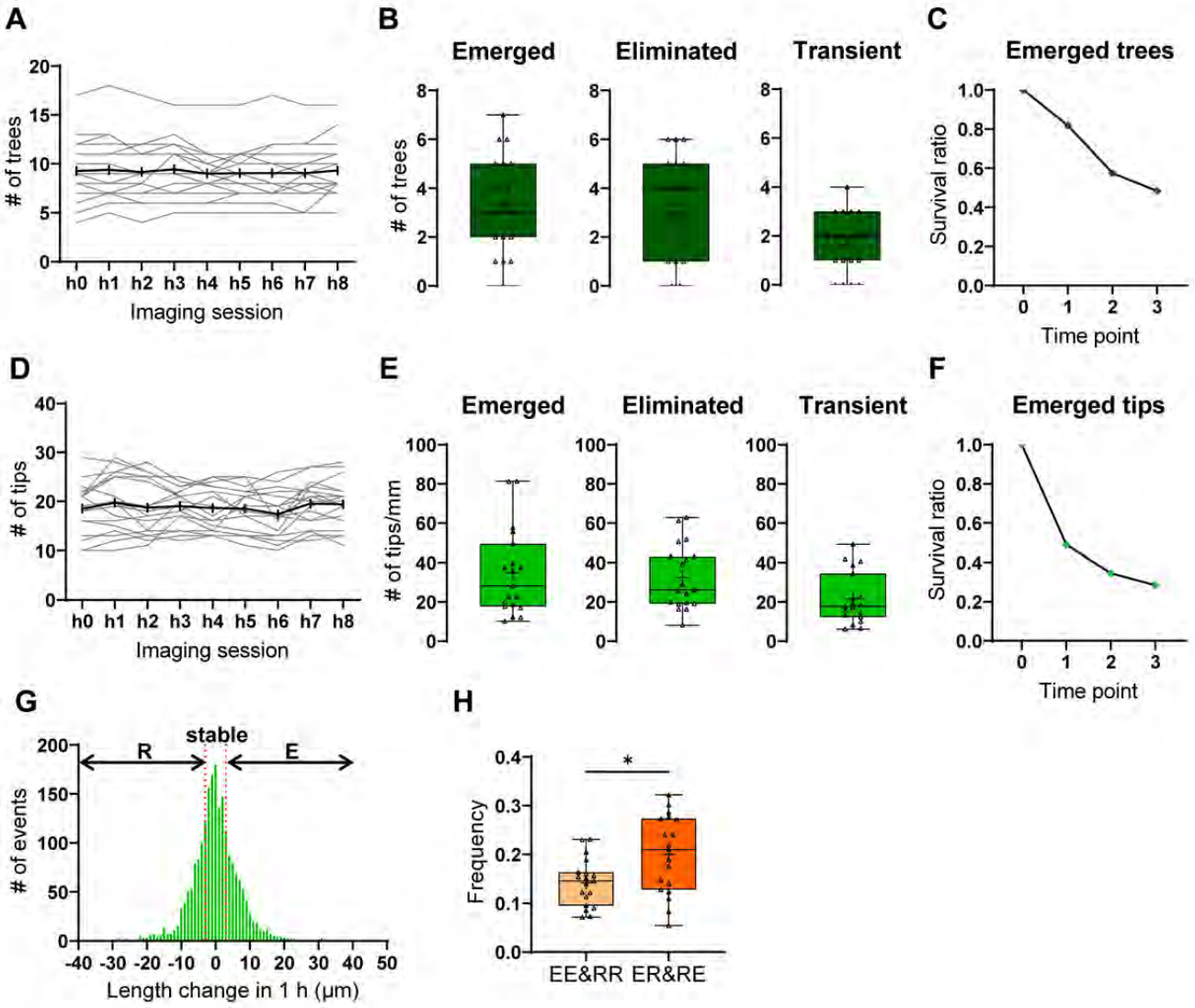


**Figure 5**

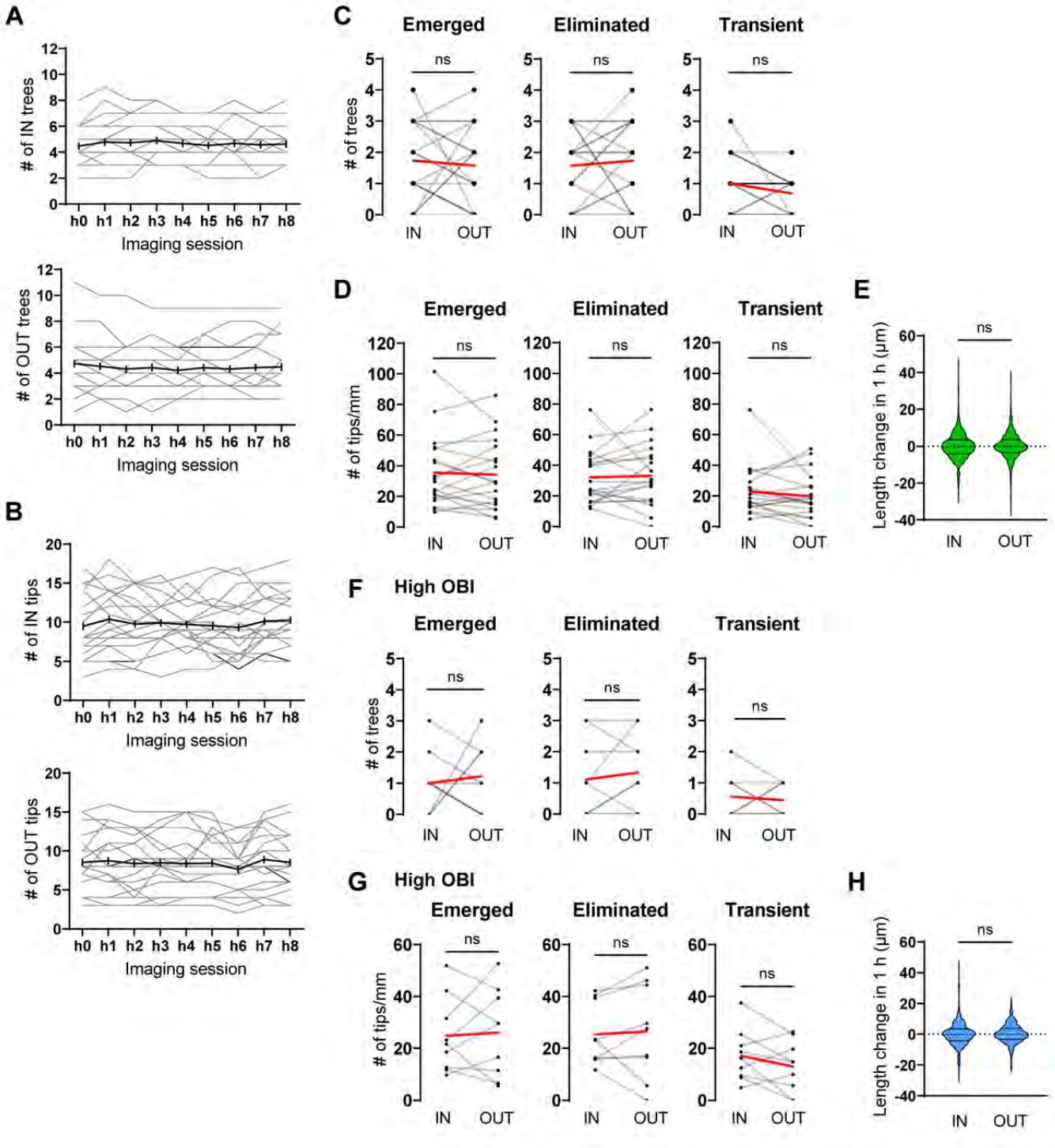


**Figure 6**

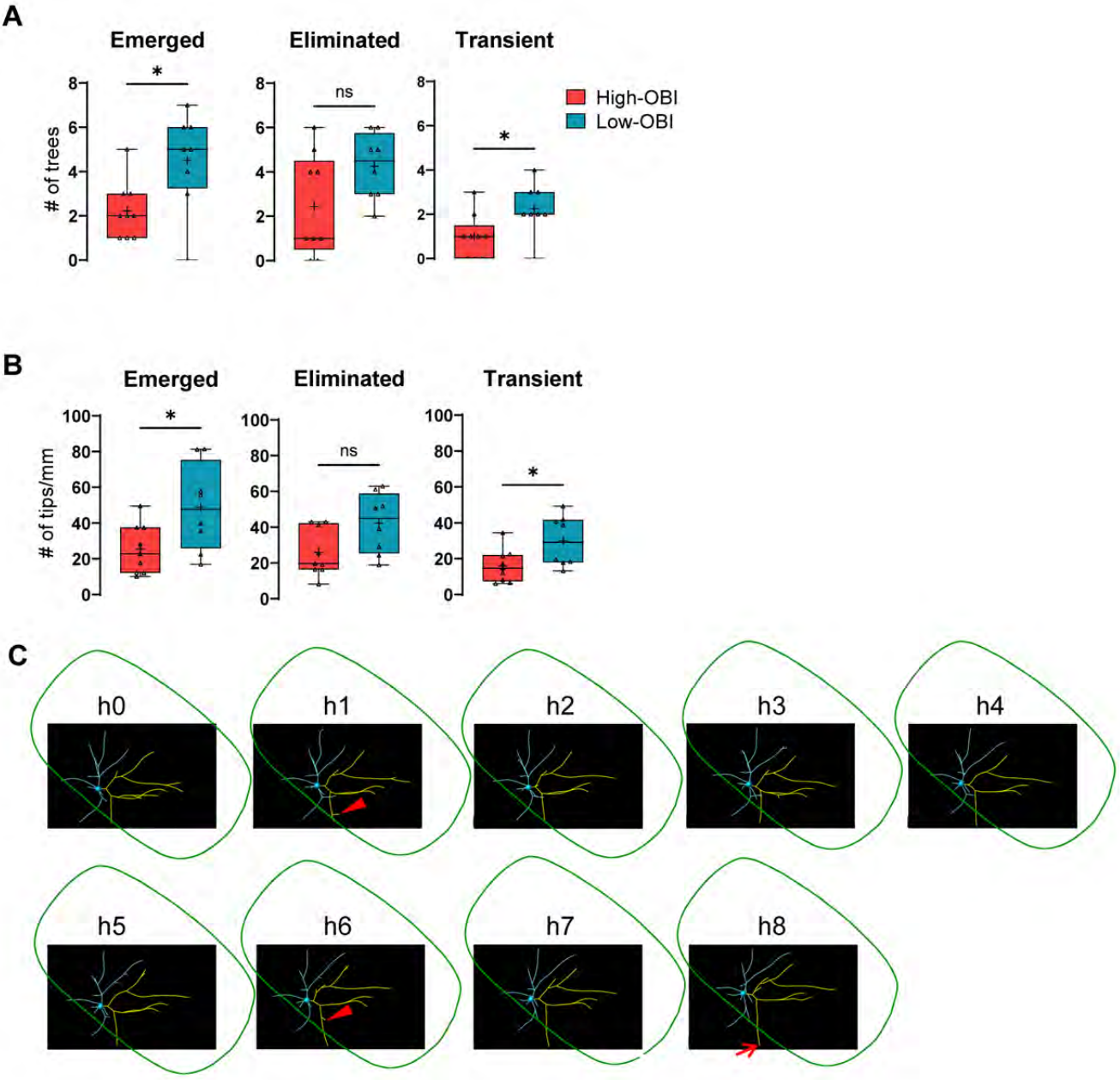


**Figure 7**

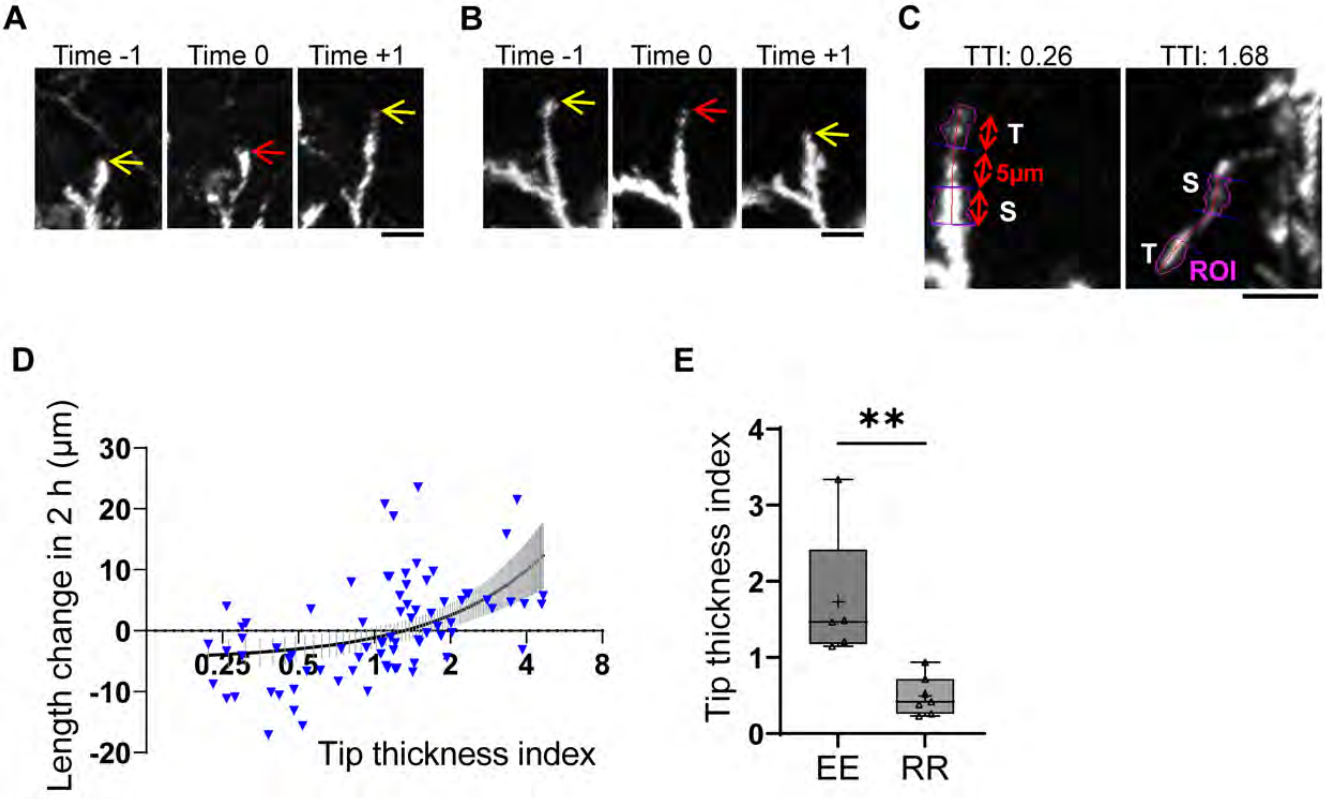


**Figure 8**

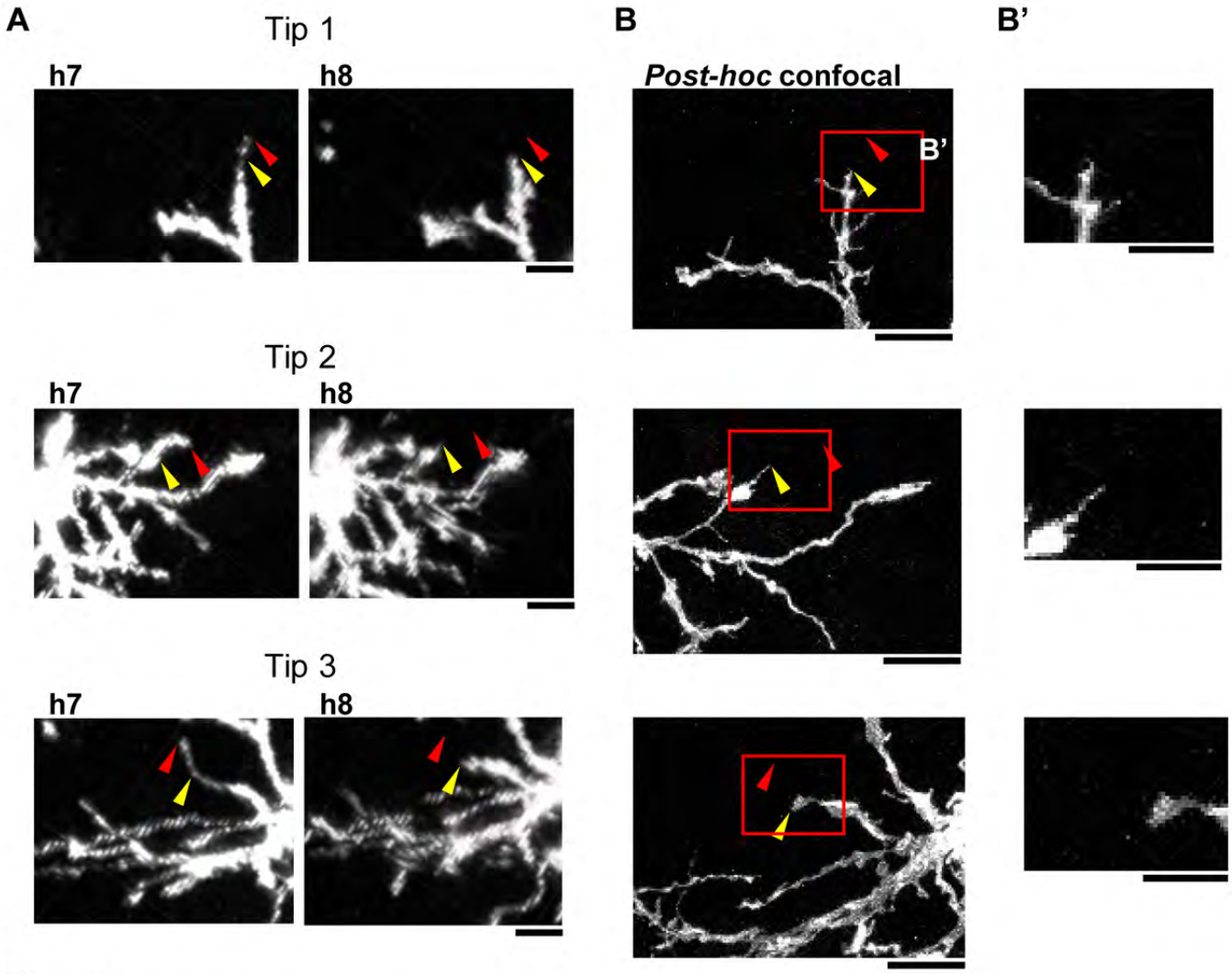


**Figure 9**